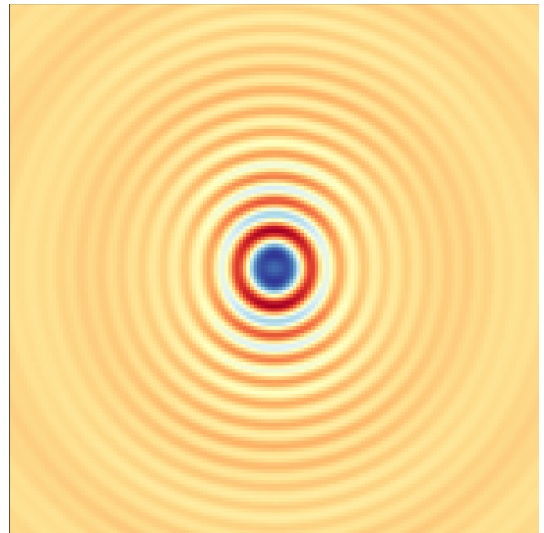
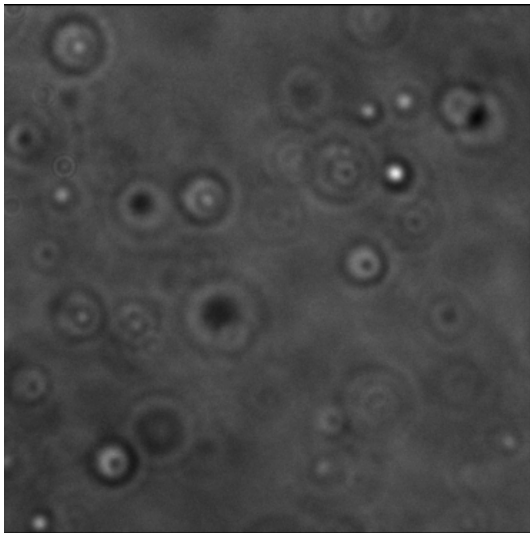




**Utrecht
University**

Thesis for the master's programme Nanomaterials Science

**Size determination and frequency response of a single
nanoemulsion droplet**



Ingmar Bruggemann BSc

Supervised by:

Anna Peters, MSc

Dr. ir. Sanli Faez

Second examiner:

Prof. dr. Allard Mosk

January 27, 2023

Nanophotonics research group
Debye Institute for Nanomaterials Science
Faculty of Science
Utrecht University

Laymen summary

Understanding properties of small particles, such as their size is important in many applications, for example in diagnostics and imaging methods. Often, the particles are dispersed in another solution, think for example of blood cells in serum. A widespread approach uses fluorescent labelling to visualize these particles, by means of chemically attaching a compound to the original particle. This causes differences in structure and how the particle moves.

Here, we present a label-free, optical imaging technique, able to detect and characterize single particles in solution. By using microscopy and computational analysis, we image the particles and try to determine their size, down to the single-particle level. In addition, an electric field was applied to a single emulsion particle and its optical response was recorded.

The size of the prepared nanoemulsion droplets was estimated to be between 100 and 150 nm. The results from the microscope show that the presented optical detection system is capable of detecting very small particles and that our method produces small and stable emulsions. The optical signal obtained from the application of the electric field was converted into a frequency response, using Fourier transformation. The results showed an expected signal at the starting frequency, but also some higher-order modes. These results serve as a first step into investigating single-particle dynamics, using straightforward experimental methods. From this point forward, other particle properties, such as their shape and response to more external perturbations could be investigated.*

*Titlepage figures represent (left) a snapshot of a nanoemulsion, in which particles are both in focus (bright spots) and out-of-focus (blur and fringe patterns). The simulated scattered electric field profile of a single sphere is displayed on the right.

Abstract

Getting a more thorough understanding of the properties of small particles (≤ 500 nm radius) is important for many fields of application, such as in biomedical and chemical research. Due to their small size (resulting in weak scattering) and rapid out-of-focus diffusion, both compromise the analysis using common microscope systems. Until now, chemical particle labelling and enhanced illumination sources (e.g., electron microscopy) have been explored. These investigate particles outside their natural environment, give unwanted background signal and by changing the structure of the studied particle, their dynamics are different. Therefore, there is need for a label-free, optical imaging technique which is easy to use and sensitive enough to resolve these particles, down to the nanoscale level.

Here, we present an optical detection systems which is able to detect single, diffusing particles. Bright-field microscopy is used to illuminate the sample and the scattered intensity is recorded on a sensitive camera. With advanced image processing, particles are located and tracked over time. In our experiments, we use self-created emulsions of oil and water in different compositions and obtain an estimate of their size(-distribution). Secondly, cross-polarization dark-field microscopy is employed to analyse the particle's optical response to an external electric field.

Pre-defined monodisperse polystyrene particles were imaged using bright-field microscopy and their intensity was measured. By using different sphere sizes, the relation between intensity and particle size was displayed. Oil-in-water emulsion droplets were investigated using computational counting and their intensity was calculated. The mean droplet intensity was transformed into a size, using the relationship between polystyrene particle sizes and intensity. Using a normal distribution fit, a size-estimate of the oil-in-water emulsion droplets was calculated to be 128 ± 10 nm. In addition, single-particle actuation of several emulsion droplets was carried out, using cross-polarization dark-field microscopy. Several modulation frequencies were applied to the particle and the response (i.e., optical signal) was recorded. From this, using Fourier transformation, the input frequency was recovered, as well as several higher-order harmonics, most likely due to non-linear particle behaviour, but further research is required to draw more decisive conclusions on this point.

The results presented in this work might serve as a starting point for further investigations into particle characterization and dynamics.

Contents

1	Introduction	6
1.1	Characterization of particles for diagnostics	6
1.2	Particle detection with optical imaging	6
1.3	Emulsion as model system for biological particles	8
1.4	Scattering behaviour and frequency response	9
1.5	Outline of this report	10
2	Theoretical and technical background	11
2.1	Illumination and imaging	11
2.1.1	Dark-field microscopy	11
2.1.2	Cross-polarization in dark-field microscopy	12
2.2	Particle motion and physics	13
2.2.1	Damped harmonic oscillator	13
2.2.2	Particle scattering: Rayleigh and Mie theory	14
2.3	Emulsion properties	17
2.3.1	Electrophoresis and shape oscillations	18
2.3.2	Electric double layer	19
2.3.3	Displacement and non-linear response	20
2.3.4	Particle size measurements	21
2.4	Analysis and simulation	21
2.4.1	Image processing using background correction	21
2.4.2	Particle counting and tracking: Trackpy	21
2.4.3	Radial averaging and periodicity	22
2.4.4	Scattering simulation	23
3	Materials and methods	25
3.1	Sample preparation	25
3.1.1	Materials	25
3.1.2	Polystyrene and emulsion samples	25
3.1.3	Flow channel preparation	25
3.2	Sample characterization using bright-field microscopy	26
3.2.1	Hardware	26
3.2.2	Software	27
3.3	Sample characterization using cross-polarized dark-field microscopy	27
3.3.1	Hardware	27
3.3.2	Software	29
3.3.3	Electronics and their function	29
3.4	Simulation for background correction	31
3.5	Particle scattering simulation: in- and output	33
4	Results and discussion	35
4.1	Particle landing simulation and data processing	35
4.1.1	Moving average and cumulative landing	35
4.1.2	Intensity cut-off	37
4.1.3	Fourier filtering	39

4.2	Experimental measurement preparation	40
4.2.1	Flow channel properties	40
4.2.2	Diluting polystyrene particles	41
4.2.3	Emulsion preparation	42
4.3	Size measurement in the bright-field microscope	43
4.3.1	Characterization of pre-defined particles	43
4.3.2	Comparison with numerical simulation	43
4.3.3	Characterization of emulsion particles	45
4.4	Experimental and simulated scattering patterns	47
4.4.1	Changing particle position in SMUTHI	48
4.4.2	Experimental particle scattering pattern	50
4.5	Characterization on the dark-field microscope	51
4.5.1	Emulsion visualisation	51
4.5.2	Emulsion actuation and analysis	51
5	Conclusion and outlook	55
	Bibliography	56
A	Pixel size calibration	59
A.1	Bright-field microscope	59
A.2	Dark-field microscope	60
B	Data and code availability	61
B.1	Comparison of extinction efficiency calculated with SMUTHI and Miepython	61
B.2	Determining the accuracy of a SMUTHI extinction efficiency calculation . .	62
B.3	SMUTHI scattering profiles for varying particle positions in a layer system .	64

Chapter 1

Introduction

1.1 Characterization of particles for diagnostics

Understanding the structure of matter, e.g., its size and shape, is important to relate function to composition. A great example is that which is present in all of us, namely the building blocks of our body: cells. In medicine, the drive to cure people is anchored around the present knowledge base of these cells. Deviations of cell function and morphological aspects, e.g., size and shape, are often key in formulating a diagnosis and establishing a cure [1]. Because the human cell consists of multiple components, we will zoom in on one and take proteins as example. Since proteins are involved in many pathways, a thorough comprehension of its properties is required, such as charge, mass, mobility and the earlier mentioned size and shape [2]. Currently, analysis is mostly performed *not* on the single-particle level, which is detrimental since morphological differences could be present, and the sample often undergoes denaturation [3]. As a result, there is a demand for techniques which are capable of characterizing single particles for various properties, while being reproducible as well. Optical imaging could be of interest to fit this need.

1.2 Particle detection with optical imaging

Developments in the field of optical microscopy have paved the way to investigate structural components, as well as dynamics up to the nanoscopic length scale. This often requires labelling particles, e.g., with fluorescent dyes [4]. Unfortunately, sample destruction and laborious methods hamper an easy-to-perform and fast investigation. Label-free technologies are therefore needed, which will be advantageous due to an absence of bleaching and blinking, simpler sample preparation and increased bio-compatibility [5]. An overview of different label-free technologies is shown in Figure 1.1. Although it seems straightforward to not label a particle and still visualize it under the microscope, the ability to detect it using standard confocal microscopy decreases. This is because illumination from the background and that which has interfered with the particle, are difficult to separate from each other [6]. Also, as the particle size decreases, its cross section, i.e., the effective area available to scatter or reflect light, decreases rapidly with the particles diameter. Hence, if the particle size decreases, it becomes more challenging to experimentally measure the relevant signal.

Besides tagging a target, being able to detect and investigate a single particle rather than in a bulk sample could provide detailed information on various processes. Studying a single protein for example, could benefit to our understanding of their complex activity in cells, such as transport and catalysis [7]. Also, being able to differentiate between benign and malignant cells is of obvious importance. The quest for single particle accuracy was boosted by implementing fluorophores to the molecule of interest, however, often a low throughput and limited field-of-view (FOV) compromises this experimentally [8].

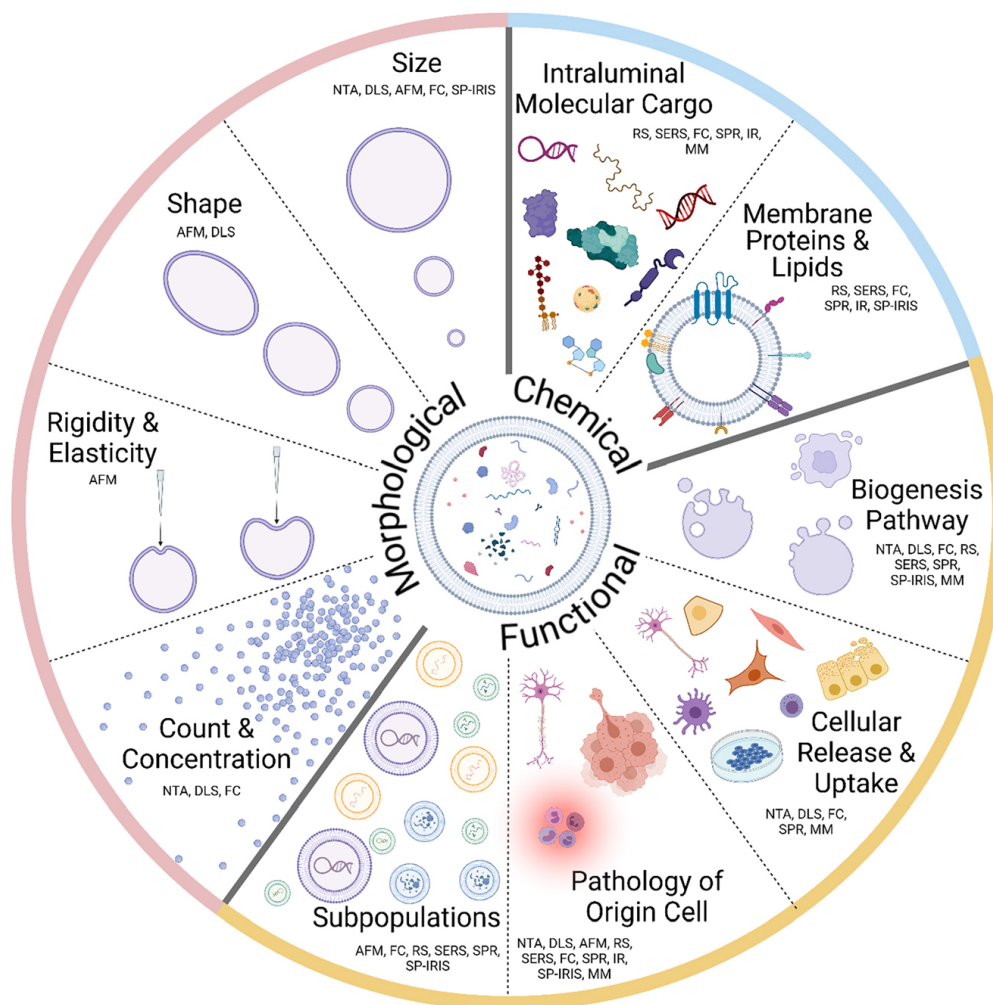


Figure 1.1: Overview of several label-free technologies to optically characterize biological particles; here extracellular vesicles. The methodology to study a specific property is placed directly below the property name, e.g., nanoparticle tracking analysis (NTA) for size and dynamic light scattering (DLS) for shape. In this work, we focus on the size using NTA. Reprinted with permission from ref. [9], licensed under the CC Attribution 4.0 (Open Access). Copyright 2022 De Gruyter.

Single-particle tracking

Furthermore, while stationary systems, such as fixed cellular samples, could be imaged with standard confocal microscopy, high dynamical systems cannot, such as when rapid diffusion takes place. A high frame rate is required, which limits the options to currently available wide-field setups. At this point, the few commercial solutions are often not applicable to obtain nanoscopic accuracy, leading to custom made optical systems [10]. A downside of using wide-field microscopy is that signal will be recorded originating from the background, i.e., not from the particle of interest. However, combining the large FOV of wide-field microscopy and emulsions with large concentrations, it is possible to overcome the current limitations of single-particle detection with wide-field microscopy.

In these high dynamical systems, being able to track specific particles or components is crucial. For this reason, two-dimensional (2D) single-particle tracking (SPT) has been developed and can be found in a broad range of (biological) applications, such as virus

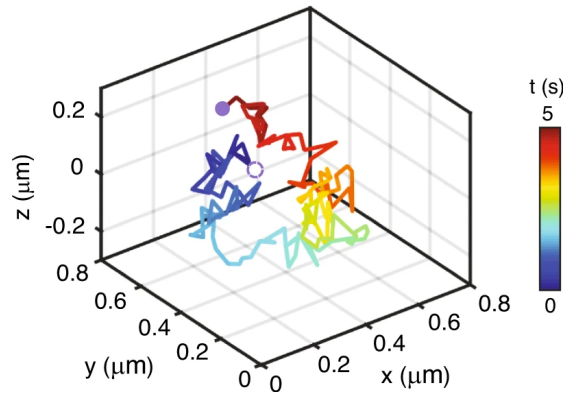


Figure 1.2: A 3D trajectory of a single quantum dot (QD). The colour bar displays the time during the measurement. The solid purple circle represents the endpoint. Reprinted (adapted) with permission from ref. [13], licensed under the CC Attribution 4.0 (Open Access). Copyright 2020 Springer Nature.

infection mechanisms, intercellular transport and membrane dynamics [11, 12]. This technique requires particles of interest to be in the focal plane and could therefore result in difficult experimental conditions to obtain sufficient signal. As a consequence, efforts into *three-dimensional* (3D) tracking have been put to overcome this limitation. One widely used approach to obtain 3D localization information is by using 2D images taken at different focal depths, so-called z -positions. High localization accuracy and low computational costs are key parameters [11]. See Figure 1.2 for an example of 3D single-particle tracking.

1.3 Emulsion as model system for biological particles

Up to this point, we discussed the possible advantages of using optical imaging to investigate biological samples. Before being able to do so, and for the scope of this thesis, we choose a generalised sample, which is broadly used as model system, namely emulsions. Due to their versatility, both in terms of composition and preparation methods, they are found in many areas of research, ranging from pharmaceuticals and cosmetics to food industry and materials science. For instance in drug-delivery, nanoemulsions can be equipped with peptides or proteins to stabilize them and allow bio-compatibility [14, 15]. Methods to produce these emulsions have been described extensively [16].

Besides medical applications, the food industry also uses the property to encapsulate certain compounds, which would otherwise degrade due to processing conditions [17]. Employment of non-destructive, label-free imaging techniques, characterization of these emulsions could help in a better understanding of their properties. Think for instance on stability, charge dynamics and diffusion [18]. By using emulsion droplets with an aimed diameter in the range 100-800 nm, conveniently called *nanoemulsions*, we want to look at single particles. Usually, their small size makes it difficult to optically inspect the particle, since the scattering intensity decreases rapidly as a function of particle size. As a solution, elastic scattering and electrophoretic properties are used to characterize a single nano-droplet [19]. An example of two types of emulsions is shown in Figure 1.3.

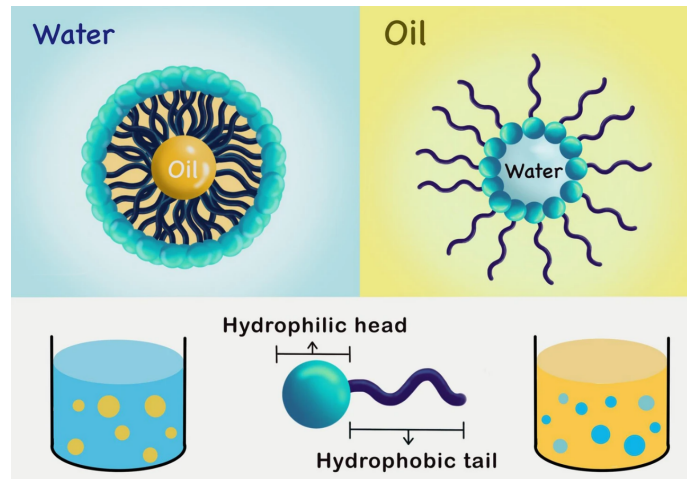


Figure 1.3: Example of an oil-in-water (O/W, left) and a water-in-oil (W/O, right) emulsion. Due to their amphiphilic nature, certain oils can form (spherical) aggregates, which could be used in experiments as particle system. Reprinted with permission from ref. [20]. Copyright 2021 Springer Nature.

1.4 Scattering behaviour and frequency response

Several techniques have been developed to relate the scattered signal after illumination to determine the particle size, for example *interferometric particle imaging* [21]. In here, an out-of-focus particle is illuminated and the scattered signal forms a fringe pattern. Since a different particle size causes a change in fringe pattern, it is possible to determine the particle size and location [22]. In this work, we investigate the scattered signal for emulsion droplets and compare the pattern to numerical simulations. Important to note here is that, for the size determination, the emulsion droplets are freely diffusing during illumination, without any external influence.

Besides investigating the scattering for particles without external disturbance, it is possible use electrophoretics, e.i., the motion of particles under the influence of an uniform electric field, to obtain properties such as the mobility and drag coefficient [23]. By using an oscillating electric field, the particle could enter an oscillatory motion and possess non-linear behaviour. See Figure 1.4 for an schematic example. Upon illumination, this motion could be expressed by a repetitive intensity change of the scattered light. After analysis (e.g., Fourier transformation), relevant frequencies are determined, which are dependent on particle size and composition [24, 25].

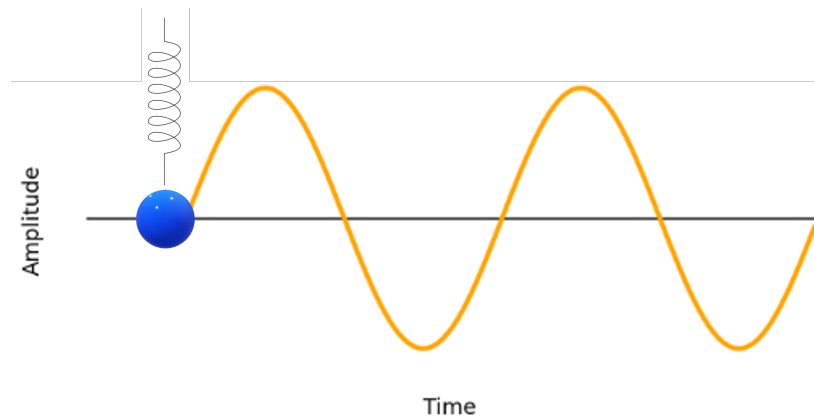


Figure 1.4: Schematic of a simple harmonic motion. A particle (blue ball) is attached to a spring and undergoes a sinusoidal oscillatory motion around the equilibrium point ($y = 0$). It has a constant frequency and amplitude.

1.5 Outline of this report

In this work, as mentioned above, we try to detect and characterize single nanoemulsion droplets, especially their size. We continue this work with a theoretical description of particle motion and scattering, in order to get an idea of the principles behind the obtained experimental images. After that, we discuss particle properties and current ways to determine the particle size in dispersion. chapter 2 ends with a detailed explanation of the variety of computational methods available to process data. In chapter 3, the used experimental methods will be discussed, with a thorough description of the analysis software designed for our system. chapter 4 will then display and discuss the obtained results for emulsion preparation, microscope calibration and the various particle measurements performed, as well as results from different simulations. It also shows the application of an external electric field on a nanoemulsion droplet. The conclusions and any other remarks are reported in chapter 5.

Chapter 2

Theoretical and technical background

In this chapter, an overview is presented of the related theory and a description of some technical equipment. There are roughly 3 parts to be distinguished here:

1. Illumination techniques and particle physics (section 2.1 and section 2.2)
2. Emulsion properties (section 2.3)
3. Image analysis and software (section 2.4)

We start with the description of illumination methods and their application in imaging experiments. Then, the physical description of particle movement and interactions with light is discussed. After that, we take a closer look at emulsion properties and the different analysis tools available to investigate experimental data and for comparison with theoretical simulations.

2.1 Illumination and imaging

2.1.1 Dark-field microscopy

One widely used imaging technique is called *dark-field microscopy* (DFM), which is able to produce high-contrast images with high resolution [26]. This microscopical method could be used in both light and electron microscopy. The name “dark field” comes from the fact that it produces an image with bright objects and a dark background, because only light that has interacted with the sample is collected. See Figure 2.1 for an schematic illustration. Light is focused through a condenser lens and illuminates the sample. Transmitted light (i.e., with no interaction) is not collected, whereas scattered light enters an objective lens and produces an image.

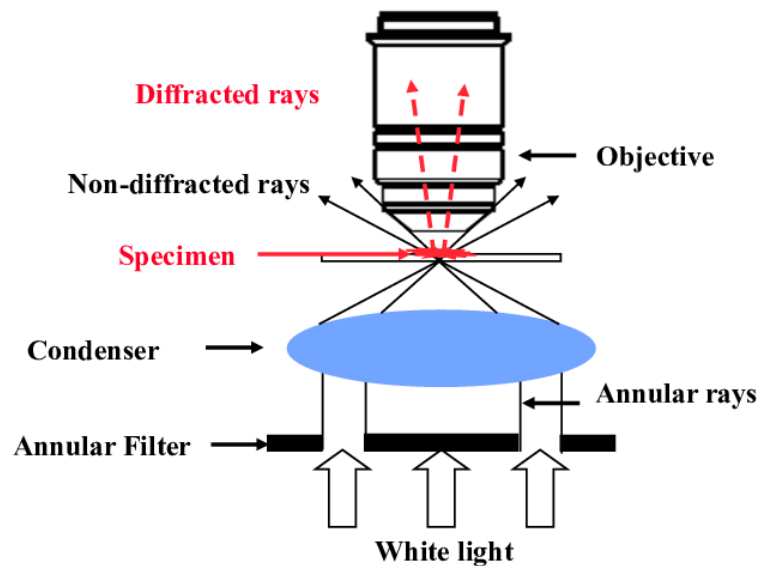


Figure 2.1: Schematic of a dark-field microscope. Only diffracted rays are used to form an image, causing the dark background. Reprinted with permission from ref. [27]. Copyright 2017 John Wiley & Sons, Ltd.

2.1.2 Cross-polarization in dark-field microscopy

Several illumination sources could be used in DFM, such as ordinary white light, a tungsten light bulb and laser light. In addition, the different polarizations of light could be used. There exist various form of light polarization:

- Linear: the electric field is confined to a single plane along the direction of incidence. When the electric field is parallel to the plane of incidence, it is denoted *p-polarized*. The perpendicular component to the plane of incidence is called *s-polarized*.
- Circular: the electric field is consists of two linear components that are perpendicular to each other, equal in amplitude, but have a phase difference of $\pi/2$. The resulting electric field rotates in a circle around the direction of propagation and, depending on the rotation direction, is called left- or right-handed circularly polarized light.
- Elliptical: the electric field of light describes an ellipse. This results from the combination of two linear components with different amplitudes and/or a phase difference that is not equal to $\pi/2$.

To understand why light polarization could be useful, we need to understand what happens with the polarization. When a light hits a flat surface, it does not change polarization, whereas a curved surface (e.g., a particle) does enforce a change in polarization. In this way, by collecting the changed polarization on a camera, the signal should originate solely from the particle. This is displayed later in Figure 3.3. Often a clover-leaf structure is obtained when imaging a particle with cross-polarization, which could be explained as follows. Single-polarized light is confined in two dimensions along the direction of propagation. This light consists of two perpendicular linear components, equal in amplitude and phase. When the x-component hits the particle, part of the amplitude will be converted into y-polarized light and another part into z-polarized light. Depending on the experimental setup, a particle could be placed in a different orientation with respect to the original (here: x) component.

Next, y-polarized light could be collected by the objective and the field distribution could be mapped out [5]. This effect is displayed in Figure 2.2.

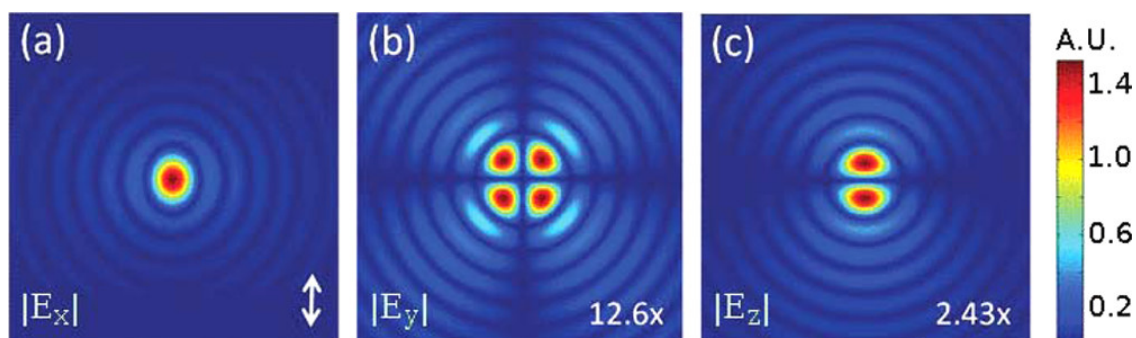


Figure 2.2: The calculated x-, y-, and z-components of the electrical field for an oil-immersion objective ($NA = 1.45$) using linear x-polarized light. The clover-leaf shape could be clearly seen in (b). Reprinted with permission from ref. [28]. Copyright 2015 American Chemical Society.

2.2 Particle motion and physics

From illumination and imaging, we continue with physical descriptions of different systems, in order to understand the observable behaviour of (single) particles in experiments. One of such a system, is the harmonic oscillator. This describes the particles response to an external disturbance. More specifically, when a system is out of its equilibrium position, it experiences a restoring force \mathbf{F} that is proportional to the displacement Δx . This model could be applied when particles are forced in motion, for instance by an applied potential or modulation frequency. In general, there are two harmonic oscillator models to distinguish: the simple model, in which there are no friction forces, and the damped model, in which these forces are present. The difference is shown in Figure 1.4. From this point onward, we will consider the damped harmonic oscillator, since this corresponds more to our situation.

2.2.1 Damped harmonic oscillator

A harmonic oscillator can be visualised as a pendulum that oscillates in ideal conditions. In such a scenario, without friction or *damping* forces, the pendulum will continue to oscillate indefinitely at a constant amplitude. However, friction forces are present, so this behaviour does not occur. A real-life example of a damped harmonic oscillator is for instance a swing. To get the swing (i.e., center of mass) out of its equilibrium state, an external force needs to be applied. When this occurs, we speak about a forced harmonic oscillator. The frequency of the oscillator changes due to this force, and changes to the frequency of the applied force. Equation 2.1 displays the conditions for this,

$$x'' + 2cx' + \omega_0^2 x = f(t) \quad (2.1)$$

where x' and x'' represent the first and second order derivative of the displacement, respectively, $c > 0$ the damping coefficient, ω_0 the systems frequency in equilibrium and $f(t)$ the forcing function. See Figure 2.3 for a graphical illustration.

Being in a forced oscillation means that an external force is applied to an oscillating system. It will not necessarily drive the system at a higher amplitude. To put this in

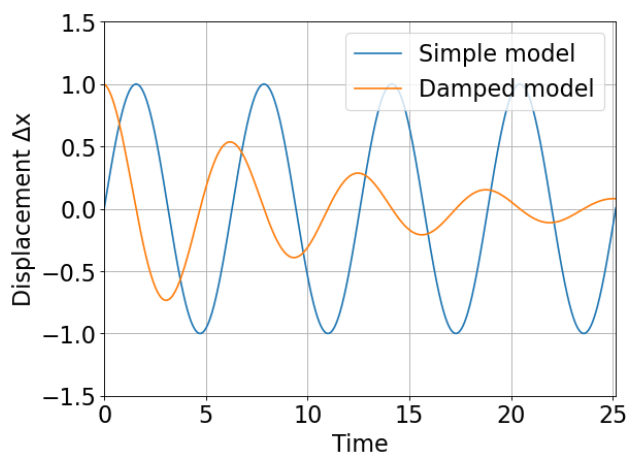


Figure 2.3: Comparison between damped (blue) and undamped (orange) harmonic oscillator. Over time, the displacement (i.e., amplitude) in the damped model decays to zero. The undamped oscillator remains unchanged.

perspective, we take a look at the swing system again; only using your legs at the appropriate time will drive the swing higher. The frequency of the applied force is crucial in determining the system's oscillatory response. At a specific frequency, the system will oscillate at its peak amplitude. The frequency for the oscillator to respond with maximum amplitude is called the *resonance* frequency. When an exerted force matches the oscillator's resonant frequency, it is said to be in resonance. Employing this resonance frequency could be used to force a particle into (an oscillatory) motion. More on this in subsection 2.3.1.

2.2.2 Particle scattering: Rayleigh and Mie theory

Besides particle oscillation caused by an external vector, other forms of light-matter interactions could occur, such as reflection and scattering. Here, we will investigate what happens when a particle encounters a light source (e.g., a laser).

When a particle collides with a ray of light, in many cases scattering occurs. This is a process in which the electromagnetic radiation is deflected or diffused, due to absorption and emission. In reflection, the incident ray bounces off a surface, under the same angle as the outgoing ray. Figure 2.4 illustrates these two effects.

A form of scattering we witness everyday is the blue sky. When the incident light from the sun hits a gas molecule, some of it gets absorbed. The blue light (having a higher frequency) is absorbed more often compared to the red light (lower frequency). After some time, the molecule radiates the absorbed light in different directions. This light is of the same wavelength as the absorbed, so mostly blue. This principle is referred to as Rayleigh scattering, named after the 19th-century British physicist Lord Rayleigh. The wavelength of the scattered light holds a relation with the particle size, which is represented in Equation 2.2,

$$x = \frac{2\pi r}{\lambda} \quad (2.2)$$

where r represents the particle's radius, λ the wavelength of the absorbed light and x the relative particle size.

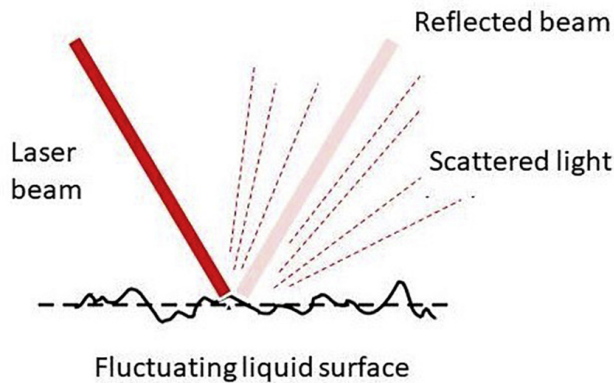


Figure 2.4: Schematic illustrating the principle of reflection and scattering upon illumination by a laser beam. Absorption and emission of the laser beams causes scattering and could occur in multiple direction. In reflection, the outgoing beam leaves under the same angle as the incoming beam, with respect to the surface normal. Reprinted with permission from ref. [29]. Copyright 2021 Elsevier.

In terms of scattering, three distinct types exist. These depend on the particle radius r and the wavelength of the incident light in the following fashion:

$$\text{Scattering type} = \begin{cases} \text{Rayleigh} & \text{if } x \ll 1 \\ \text{Mie} & \text{if } x \simeq 1 \\ \text{Geometric} & \text{if } x \gg 1 \end{cases}$$

In this work, we aim for particles in the size between 50 nm and 500 nm. Following Equation 2.2, this means that Mie scattering is prone to occur.

Mie theory refers to the scattering of an electromagnetic plane wave by a homogeneous sphere, and is mathematically expressed as an infinite series of spherical multipole partial waves. It is often encountered when investigating spherical shapes, but could also be extended to cylinders for example. By solving the mathematical expression, a scattering profile is obtained: a detailed expression of the direction and magnitude of the scattered field. A parameter that is involved in this scattering profile, is called the cross section: the total area that is illuminated. Several *cross sections* exist, but below we focus on the *geometric* cross section and the *scattering* cross section.

For spherical particles, their geometric cross section is calculated as a function of their radius and shown in Equation 2.3,

$$\sigma = \pi^2 r \quad (2.3)$$

where r represents the particles radius and σ the geometric cross section.

Following Mie theory, light interactions, such as scattering, have shown to possess a different scattering cross section, compared to the geometric cross section. The scattering cross section of a spherical particle is dependent on the geometry and refractive index, as well as the wavelength of the used light. Usually, the scattering cross section is calculated using *efficiency coefficients*, which divide the, in this case, scattering cross section by the geometric cross section. See Equation 2.4,

$$Q_{sc} = \frac{\sigma_{sc}}{\sigma} \quad (2.4)$$

where Q_{sc} denotes the scattering efficiency coefficient, σ_{sc} the scattering cross section and σ the geometric cross section. The scattering cross section σ_{sc} is defined and shown in Equation 2.5,

$$\sigma_{sc} = \frac{W_{sc}}{I_{inc}} \quad (2.5)$$

where W_{sc} denotes the energy flow through the surrounding surface and I_{inc} the intensity of the incident wave.

Since an experimentally derived value for the σ_{sc} is practically impossible to obtain, numerical packages are used to calculate the scattering profile of single particles (e.g., SMUTHI, described in section 3.5) and the scattering efficiency for different particle sizes. For two of these numerical packages, called Miepython and SMUTHI, a plot of the scattering efficiency coefficient versus particle size is shown in Figure 2.5.

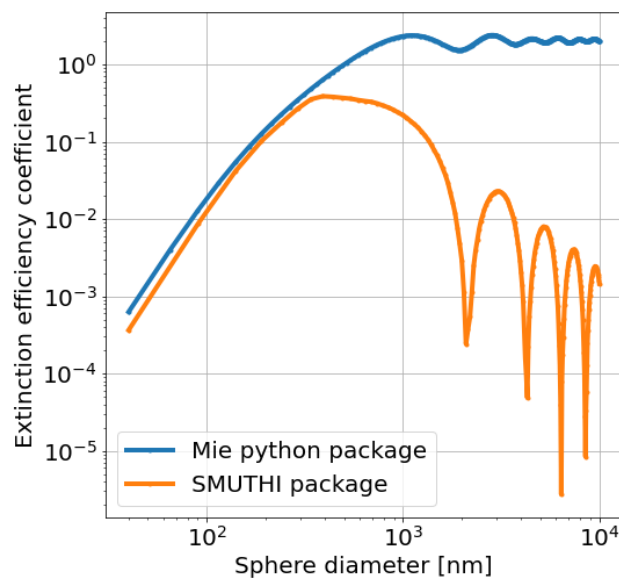


Figure 2.5: A numerical comparison of the scattering efficiency coefficients for different particle sizes. The difference between the two packages will be discussed in subsection 4.3.2.

In addition to the scattering data obtained with a simulation, the particle position with respect to the focal point determines to great extent the scattered pattern (e.g., with interference fringes). By changing the position of the incoming wave, we can simulate the profile when the scattering occurs due to under- and overfocussing, see Figure 2.6. Note that for our system, the particles are diffusing in a flow channel, causing a different position over time, while the objective is kept in a fixed position. This means that an image contains both particles in the focused position, as well as out-of-focus patterns (fringes and blurs).

When particles are stuck to a glass surface, it is possible to move the objective (i.e., focal point) and get an estimate of the *focal depth*, the distance between the top and bottom substrate. This is shown in Figure 4.7.

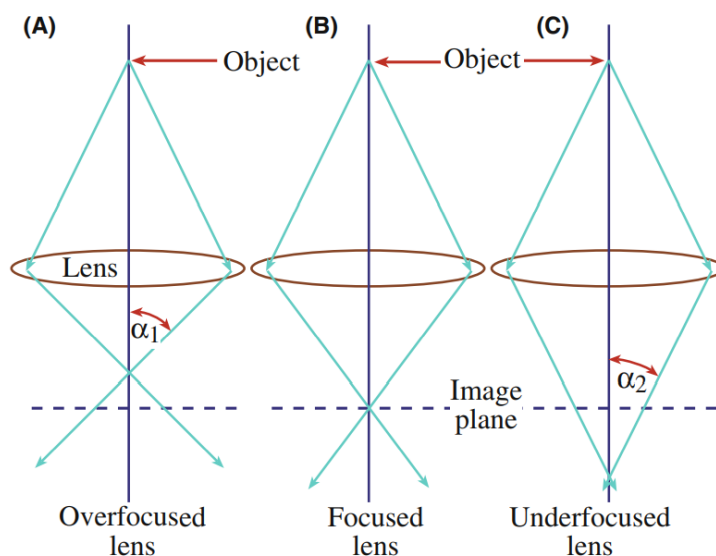


Figure 2.6: (a) a too strong lens focuses the rays above the normal image plane, resulting in overfocussing and interference fringes. (b) the rays from the object are focused on the image plane, creating a sharp image. (c) the opposite of overfocus, in which the lens is too weak, placing the object ray below the image plane and causing a blurry image. Reprinted with permission from ref. [30]. Copyright 2009 Springer Nature.

2.3 Emulsion properties

Now that we have an understanding of some of the physical interactions that are related to our work, we zoom in on emulsions. As mentioned in chapter 1, we aim to characterize a single nanoemulsion droplet, which function as model system for biological particles. Here, some properties of emulsions are explained in more detail.

An emulsion is best described as a physical system in which two immiscible liquids are present. One liquid is called the internal phase, the other is called the external phase. In emulsions, the internal phase is dispersed in the external phase. In a dispersion, simply described, particles are mixed. In the case of emulsions, the two particles are in liquid phase. Other examples of dispersions are gels (liquids dispersed in solids) and aerosols (liquids dispersed in gasses). We will now focus on an emulsion, so containing two liquids.

Normally, these two liquids do not mix and a two-layer system is formed. However, there are some ways to create an emulsion. A distinction is made based on the relative amount of energy used (i.e., low and high) and this results in four main methods to create nanoemulsions. These are listed below and each method is briefly described. Method 1 & 2 represent low-energy and method 3 & 4 high-energy [31]. Here, W/O denotes water dispersed in oil, and O/W oil dispersed in water.

1. Phase-inversion temperature (PIT): a W/O emulsion at high temperature is cooled to room temperature, passing the inversion temperature. At this point, the oil-water interface tension is low, resulting in O/W emulsion particles with high specific surface area.
2. Inversion point (IP): water is slowly added to a W/O emulsion. At the inversion point, the oil-water interface tension is low and the emulsion becomes O/W with small particles.

3. Ultrasonication (US): high frequency sound waves are used to agitate particles in solution, causing disruption due to shear stress and lead to small particles.
4. High pressure homogenization (HPH): an O/W emulsion containing large particles is pressed through a small gap by a pump. The gap size is usually in the micron range and repetition (with smaller gap sizes) creates small particles.

Even though these methods could be used to form a nanoemulsion, the processes are non-spontaneous, which means that eventually the emulsions will return to the initial state in which the two phases are separated. The rate at which this occurs varies greatly, e.g., consumer milk will remain stable for a long period of time, while coffee cream will rapidly evaporate [32]. To slow down this effect, one could add an emulsifier. Such a compound could form a layer around the dispersing phase, making it able to “survive” in close contact with the external medium, therefore called a *surfactant*. Emulsions could also be prepared by manual shaking a bottle of two liquids. Dependent on the intensity and duration of shaking, the particle size could be decreased.

2.3.1 Electrophoresis and shape oscillations

From this point onward, we will discuss the possible interactions of (emulsion) particles with an external electrical potential or frequency. It is known that particles could undergo a motion when an external electric field is applied. This principle is referred to as *electrophoresis*: the motion of dispersed particles relative to a fluid under the influence of a spatially uniform electric field. See Figure 2.7 for an illustration.

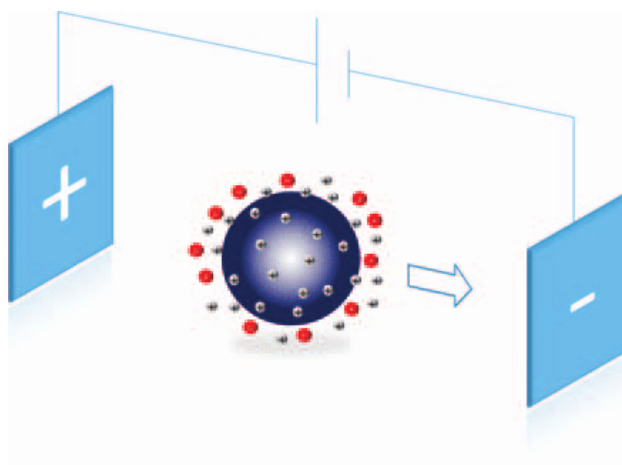


Figure 2.7: Schematic principle of electrophoresis. A charged particles moves to one electrode, and the direction (visualized with the arrow) and speed depends on the applied electric field. Reprinted with permission from ref. [33]. Copyright 2014 Royal Society of Chemistry.

Besides the movement of particles through a medium, the droplet shape could get affected by the electric field. An understanding of this effect, commonly referred to as *drop oscillations*, could be beneficial for developments in the fields of liquid displays and lenses [34]. See Figure 2.8 for an illustration of this effect.

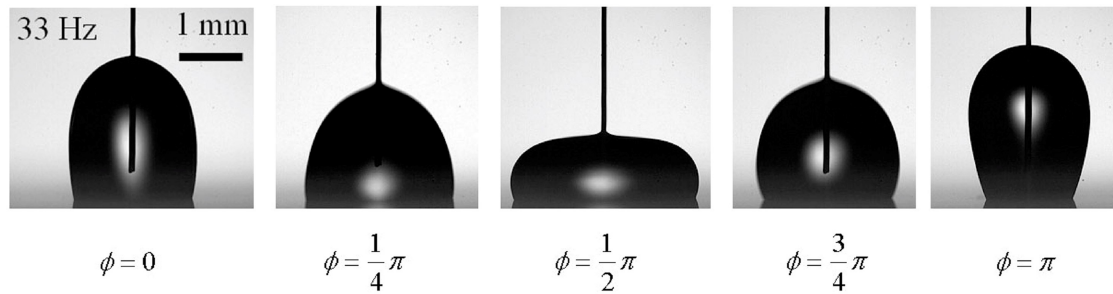


Figure 2.8: A sodium chloride droplet placed on an isolated ITO cover glass undergoing droplet deformations. The input frequency and voltage were set at 33 Hz and 60 V, respectively. The ϕ value denotes the phase angle of the input voltage and a complete period ($0 \rightarrow 1$) is shown. The vertical line in the center of the droplet represents the top electrode. Reprinted (adapted) with permission from ref. [34]. Copyright 2008 American Chemical Society.

2.3.2 Electric double layer

When an electrical potential is applied to an emulsion particle, an electrical double layer (EDL) is formed. This physical phenomenon occurs on the interface between a solid (in this case the droplet shell) and a surrounding liquid (i.e., water). Slightly negatively charged electrolytes are surrounded by water molecules and stick to the surface. So, ions in the colloidal suspension form one layer, and electrons on the electrode form the second layer. By applying an electric potential, diffusion of ions occurs and hence charge displacement. An example of the surroundings of a charged droplet is displayed in Figure 2.9.

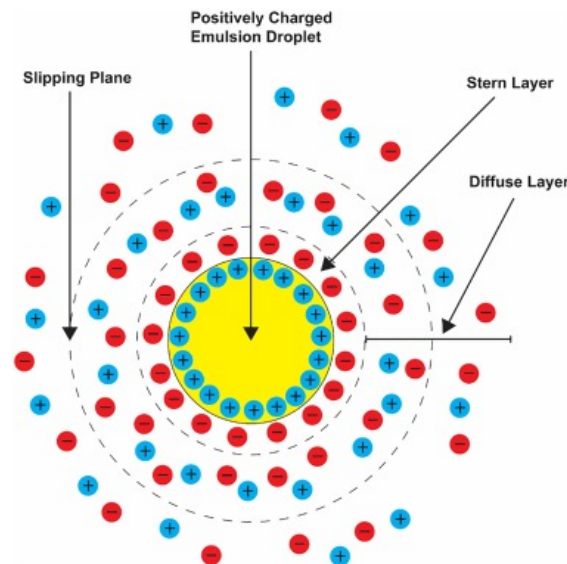


Figure 2.9: Schematic of the electrical double layer surrounding a positively charged emulsion droplet. Reprinted with permission from ref [35], licensed under the CC Attribution 4.0 NC ND (Open Access). Copyright 2022 Elsevier.

2.3.3 Displacement and non-linear response

Electrophoresis or other external perturbations might cause a change in the spatial coordinates of a single particle. With these values, it is possible to calculate the displacement, which could be further used to characterize a particle (composition). Therefore, it is necessary to know the relationship between displacement Δx , particle frequency ω and the applied electric field E . In formula:

$$\Delta x \propto E \propto \epsilon_0 \cdot \sin \omega t \quad (2.6)$$

$$\Delta x \propto E^2 \propto \epsilon_0 \cdot \sin^2 \omega t \propto \epsilon_0 \cdot \sin 2\omega t \quad (2.7)$$

$$\Delta x \propto E + E^2 \quad (2.8)$$

One way to determine the appropriate model is to apply a frequency to the particle (e.g., 50 Hz) and measure the amplitude of the optical response over time. Next, by taking the Fourier transformation, any frequencies present in the signal could be recovered. When the results show a single peak at the input frequency (i.e., 50 Hz), Equation 2.6 applies. If there is also a second peak at twice the frequency (i.e., 100 Hz), a combined response exists, as shown in Equation 2.8. Imagine an optical signal in which two frequencies are present: the input frequency at 1 Hz and a second frequency. Taking the Fourier transformation of this signal will reveal the two frequencies, as illustrated in Figure 2.10.

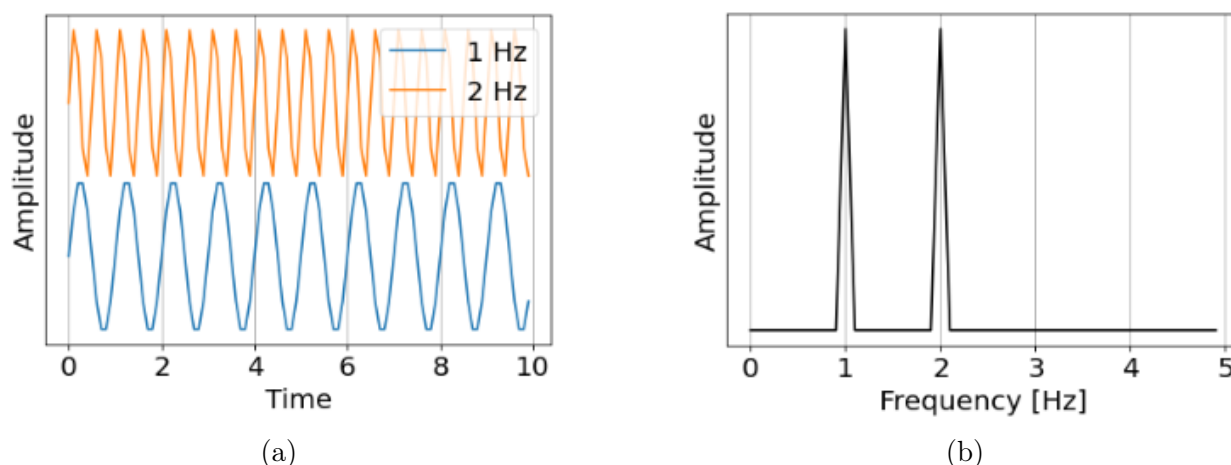


Figure 2.10: (a) Sine waves with similar amplitude, but different frequency propagating through time. (b) Fast Fourier transform of the two waves in (a). The peaks represent the frequency of the individual sine wave.

The existence of higher-order frequency peaks is referred to as *non-linearity*: a change in system input is not linear to the change in system output. Non-linearity is studied across many fields, because it could be used in systems which cannot be described with linear relationships [36]. In our situation, possible non-linear response are affected by several particle parameters, such as the size, shape and the *Young's module*, since it determines the resonant frequency at which a particle begins to oscillate. This mechanical property displays the amount of tensile strength of a material when a force is applied. Large values are obtained for materials that have a high strength resistance, i.e., do not stretch out much. In turn, the Young's module depends on particle composition.

2.3.4 Particle size measurements

The formation of nanodroplets could be confirmed by characterizing the emulsion. Normally, when analysing particles for their size, the average droplet radius could be analysed with dynamic light scattering (DLS). By using a laser as monochromatic light source, this technique measures the intensity of scattered light after hitting the droplets. Every particle is illuminated and therefore provides a scattering signal. This diffracted light will either undergo destructive interference (extinguish) or constructive interference (increase in intensity). As the particles move over time due to Brownian motion, this intensity also varies. It is this difference that allows to retrieve information about the system, in terms of size for example. Repetition of the illumination operation reduces error and artifacts and increases the validity of the data retrieved. Unfortunately, particle size determination using DLS is hampered, when the polydispersity of the created emulsion is too high. This means that the particles present in the emulsion are broad in size, which makes it difficult to assess the size of an individual particle. To overcome this, we will use advanced image processing methods to image individual particles and determine their size with high sensitivity.

2.4 Analysis and simulation

At this point, the underlying principles of particle scattering and emulsions have been discussed. To obtain useful data from the experiment, different software packages and image analysis procedures could be used. In this section, the different possible approaches are discussed, such as background correction, radial averaging and scattering (simulations).

2.4.1 Image processing using background correction

Background correction (BGC) is the process of modulating background signals retrieved from a system, often with the goal of reducing or removing noise from the data. From the microscope, a series of frames (images) is obtained. When a particle is near the focal plane, it will scatter and appear in the frame. When these frames are combined to form a series, these particles appear as if they are landing. In the last frame, all the bound particles are visible assuming no particles leave the focal area. By subtracting a subsequent frame from the previous one, it is possible to get an image, in which particles are visible with increased contrast. See Figure 2.11 for an example. This makes background correction a powerful tool, especially when particle counting and tracking during diffusion in the flow channel is required. In section 3.4, the used methods are explained to greater extend.

2.4.2 Particle counting and tracking: Trackpy

After the frames have been corrected, it is time to find the particles of interest. Since manual assessing a frame is prone to error and would give non-reproducible results, a computational tool could be beneficial to process a large dataset (i.e., multiple frames in one batch). One of such is called Trackpy*. With this tool, frames could be read and pre-defined blob-like features, such as the brightness and pixel size could be used to locate particles matching those criteria. Trackpy uses the algorithms proposed by Crocker and Grier [38]. It works in the following fashion. First, feature coordinates are obtained using the earlier mentioned selection parameters. Then, the coordinates are *linked* in time, resulting in a particles

*soft-matter/trackpy: Trackpy v0.5.0

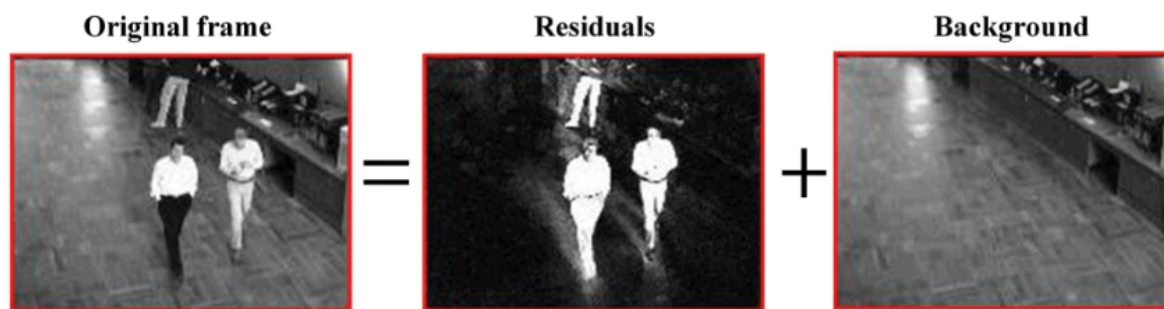


Figure 2.11: Principle of background subtraction. By subtracting the current frame from the previous one, (most of) the noise is removed, leading to only the wanted pixel data. Reprinted with permission from ref. [37]. Copyright 2018 IEEE.

trajectory. This step requires inserting a maximum feature displacement value. For dispersed particles, this frame-to-frame displacement could be large, making this parameter important, to avoid features to be counted more than once, resulting in a too high particle count. From the linking, particles could be tracked over time. From the analysis, particle brightness (i.e., intensity) and counts could be used for estimating the polydispersity (in size) and concentration of a sample.

2.4.3 Radial averaging and periodicity

Besides assigning an intensity value to a particle in focus, it is possible to investigate the shape of particles out-of-focus, especially when they give rise to *fringe* pattern. These fringes are visible in scattering patterns as rings. One way to determine the characteristic profile from a particle scattering profile, both from an experimental image as well as a theoretical simulation, is to use *radial averaging*. This is a mathematical calculation which determines the radial profile of any image pattern. By choosing the center of the particle, either manually or by using a script, the calculation searches from this center point radially outwards. At the center point, the radial distance is equal to zero and the intensity at that point functions as starting value in the plot. The calculation continues by increasing the distance from the center to the outside with a chosen step size. For instance, when this step size is equal to one, all pixel values located at a radial distance of one will be selected. An average will be calculated of all the values at this distance. In this way, a plot could be constructed in which the radial distance r is displayed against the intensity I . See Figure 2.12 for an illustration.

Since the scattering pattern contains repetitive fringes, Fourier transformation could be used to find the “oscillation” frequency of this pattern. Fourier analysis operates by expressing a function into a sum of periodic components (sine and cosine functions) and changes signals from the time-domain to the frequency domain. This operation could be applied to a 1D dataset, but could also be extended to 2D data. It could be used to describe the unique frequency, amplitude and phase ϕ of a signal. The phase property is valuable and could be used to reconstruct a signal [39]. This information is also expressed in the Fourier transform and the oscillatory pattern could be used to calculate the “phase angle”. One angle corresponds to one given oscillation of the phase. As we shall see in the next chapter, the sharp change in the phase ϕ as a function of frequency near resonance could be used to characterize a pattern.

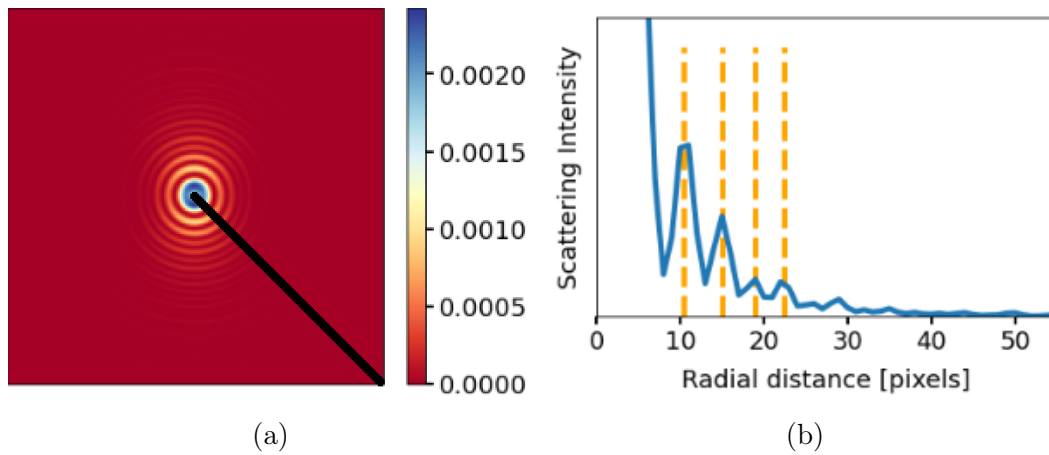


Figure 2.12: Principle of radial averaging. (a) a simulated scattering intensity profile, where the color bar represents the intensity. The black line represents the “radial” path on which the averaging occurs, starting in the center point. (b) the result of the radial averaging. The dashed orange lines highlight the peaks or *fringes*, that are present in (a).

2.4.4 Scattering simulation

SMUTHI

The previously described Mie scattering theory could be explored using numerical simulations. One of such methods is called *SMUTHI*, which stands for Scattering by Multiple particles in THIn-film systems. It could be used to investigate the (scattering) behaviour of particles in layer interfaces, such as the experimentally used flow channels. See Figure 2.13 for a schematic of the basic principle. It uses the *T-matrix* method, in which boundary conditions are matched to solutions for the Maxwell equations to obtain matrix elements. For our project, we use SMUTHI to simulate the electric field profiles for our particle system. It is possible to calculate the electric field for particles that have a specific size, shape and location in the layer system. In section 3.5, the used scripts are explained in more detail.

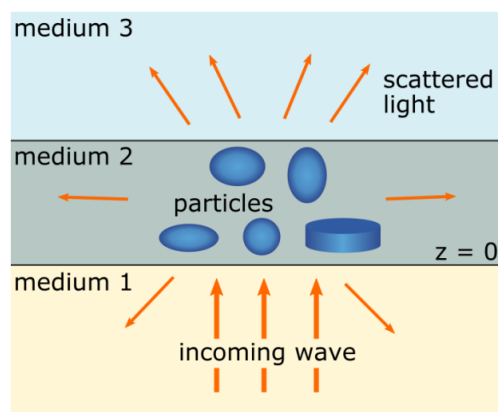


Figure 2.13: Schematic illustration the working principle of the SMUTHI software. It is build as a layer system in which particles of different sizes, positions and refractive indices could be placed. Reprinted with permission from ref. [40]. Copyright 2022 Elsevier.

Miepython

Besides SMUTHI, another package could be used to calculate the scattering of single particles, namely *Miepython*. The great difference is that *Miepython* is focused on a particle, without a layer system present. It is based on Mie theory and is used to calculate light scattering by spheres. The underlying principle is based on ref. [41]. In the coming chapters, we use *Miepython* simulations to compare with both SMUTHI and experimental scattering results. See Figure 2.14.

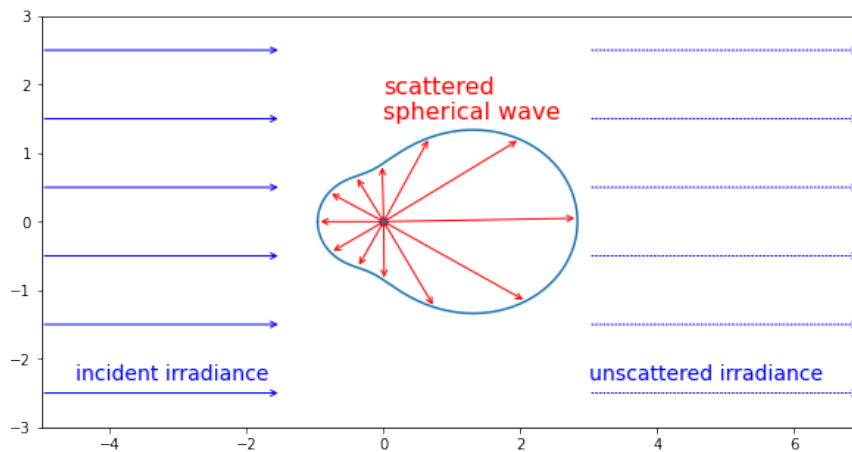


Figure 2.14: Principle of spherical scattering used in *Miepython*. Reprinted with permission, licensed under the MIT licence. Copyright 2017-2021 Scott Prahl.

Chapter 3

Materials and methods

In this chapter, all used methods are discussed. We start with a description of the used samples: polystyrene particles and (nano-)emulsions. Polystyrene is used, because it has a known predefined size, in contrary to the created emulsions. It could therefore act as reference material. After that, the microscope setups are explained, followed by the different data analysis approaches.

3.1 Sample preparation

3.1.1 Materials

Microscope slides (24x40 mm, borosilicate) were purchased from Brand and cover glass (22x22 mm, borosilicate) was purchased from VWR. ITO coated glass slides (24x40 mm) were purchased from SPI. Polysorbate-20 (Tween-20, Sigma Aldrich) and heptane ($\geq 99\%$ pure, Honeywell) were used from the chemical lab inventory. Deionized water came from a Direct-Q 3 UV Water purification system (Merck).

3.1.2 Polystyrene and emulsion samples

Polystyrene Polystyrene particles of different sizes (0.1, 0.3, 0.8 μm mean particle diameter) were purchased from Sigma Aldrich. Larger 1.58 μm fluoresbrite microspheres (Polysciences) and 3 μm latex beads (Sigma-Aldrich) were also used. Different samples were prepared by dilution with deionised water.

Emulsions

- Oil-in-water emulsions were prepared in two steps. First, deionised water, octane and polysorbate-20 were added to a glass vial in a 100:10:5 ratio (v/v/v). Then, manual shaking during 1 minute was performed, followed by placement in a sonicator (Emmi-05ST Emag) for 20 minutes took place.
- Water-in-oil emulsions were prepared by mixing and manual shaking dodecane, dionised water and sorbitan oleate (span-80) in a 100:10:4 ratio (v/v/v)

3.1.3 Flow channel preparation

A flow channel is used to create a reproducible sample holder, in which a sample could be introduced and the particles can *flow*, causing dynamical behaviour. Cover glass slide (22x22) and bottom glass slide (24x40) were cleaned by rinsing with water, ethanol and water, consecutively, after which the slides were air dried with compressed nitrogen gas. Double-sided sticky tape (75 μm thick, Tesa) was cut with a scissor and placed on the 22x22 glass slide, which was then placed on the bottom glass slide. With a pair of tweezers, any air bubbles in the sticky tape were pressed out to firmly stick the two glass slides together.

Following the same cleaning procedure, instead of using double-sided tape, parafilm was cut and stretched as far as possible. With care, the stretched pieces were placed on the cover glass slide and the cover glass was placed on the bottom glass slide. Next, the pieces were transferred to a hot plate (VWR), turned on at 200 °C. After a few minutes, the strips of parafilm were pressed upon with a pair of tweezers to even further stretch out the material (see Figure 3.1). After this, the flow channel was removed from the heat source and placed in ambient air to cool down, after which sample was introduced.

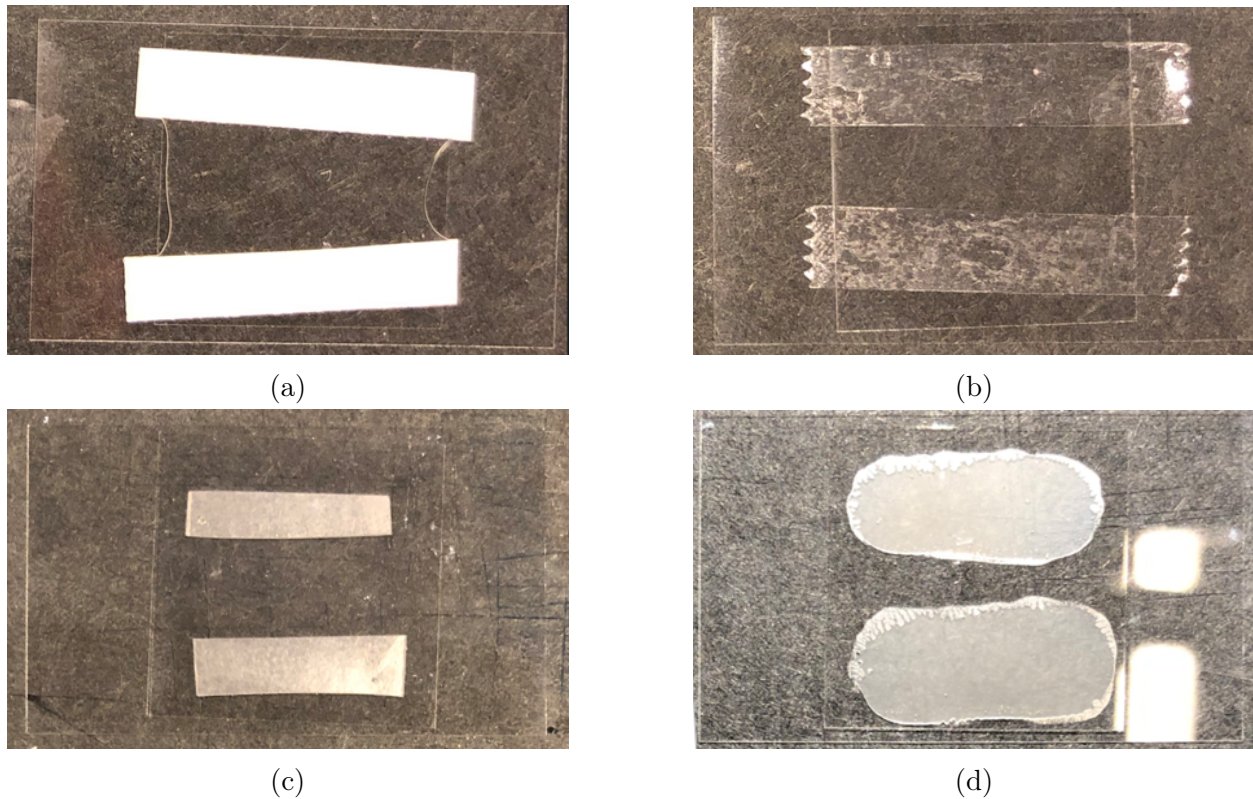


Figure 3.1: Flow channel preparation with double-sided tape of (a) 270 μm thickness, (b) 75 μm thickness and parafilm strips, before (c) and after (d) applying heat on the hotplate. The thickness of the parafilm was determined by changing the focal point and is displayed in Figure 4.7.

3.2 Sample characterization using bright-field microscopy

3.2.1 Hardware

The custom build bright-field (BF) microscope setup consists of a Hamamatsu OrcaFlash 4.0lt C11440 digital CMOS camera, with a 131x131 μm field of view and 2048x2048 pixels. Furthermore, a Thorlabs NanoMax TS MAX300 Series 3-axis flexure stage is used to move the sample holder. LED (white) light is used as illumination source. The pixel size was determined with a Thorlabs R1L3S2P calibration stage and resulted in 64 nm per pixel. See Figure A.1 for an overview of the relevant pixel data for this calibration. A schematic of the BF-setup could be found in Figure 3.2.

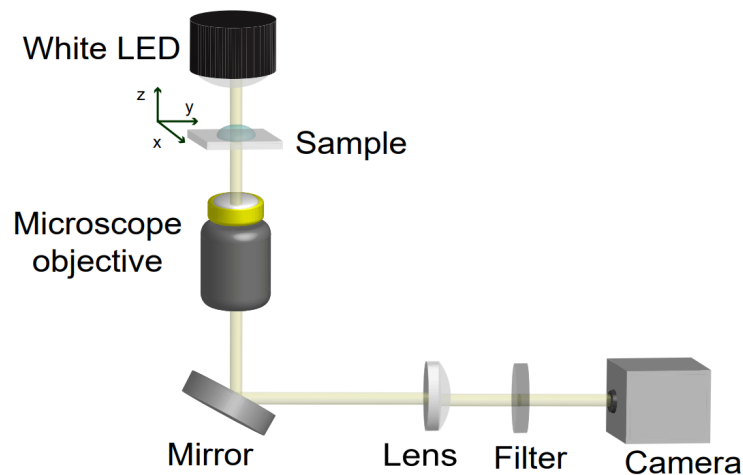


Figure 3.2: Schematic of the bright-field microscope. White LED illumination reaches the sample (i.e., flow channel), which can be moved in (x,y) direction. Scattered light is collected on the objective, which could be moved in the z -direction. The signal then propagates through a lens and reaches the camera.

3.2.2 Software

Image visualisation took place with either the camera manufacturer software HoKaWo (Hamamatsu), or with the software developed in the research group, called PyNTA: Python Nanoparticle Tracking Analysis. PyNTA is discussed later on, see subsection 3.3.2.

3.3 Sample characterization using cross-polarized dark-field microscopy

3.3.1 Hardware

The custom build dark-field (DF) microscope setup is displayed in Figure 3.3. In here, p-polarized light illuminates the sample via a polarising beamsplitter. The light interacts with the sample and the scattered light (with a different polarisation) travels to the camera. Reflected light (with unchanged polarisation) is filtered out by the beamsplitter. The pixel size corresponds to 50 nm per pixel. See Figure A.2 for an overview of the relevant pixel data for this calibration.

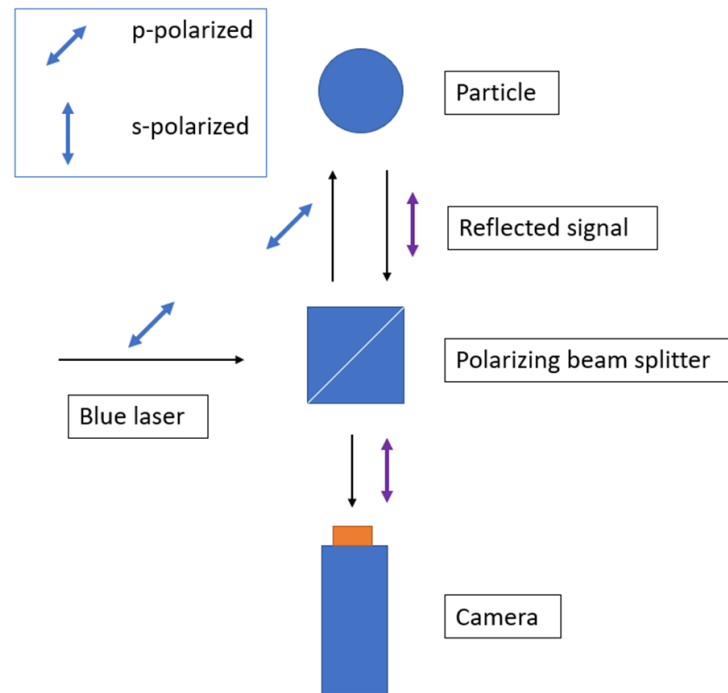


Figure 3.3: Working principle of cross-polarization. P-polarized light enters the system and reaches the particle. Upon interaction, part of the incident light reflects, without changing polarization. Another part is scattered and propagates with a 90° rotation, referred to as s-polarized.

The whole dark-field setup is displayed in Figure 3.4. Here, besides the primary, blue laser, another laser is shown. This secondary (red) laser is used to maintain focus during the experiment. Since the particles possess a small displacement (e.g., jiggling), it is important to keep the moving particles in focus. The focus lock measures the displacement of the incident beam relative to the calibrated centre and creates a feedback loop. Whenever the beam deviates, for instance because the particle is moving to the left, it acts as a feedback mechanism and restores the beam to the centre again. In this way, the particle is kept in the specific surface area (z-position) of focus, ensuring the experimental conditions (relatively) the same throughout. The dichroic mirror separates light based on the wavelength, ensuring red light to propagate in another direction compared to the blue light.

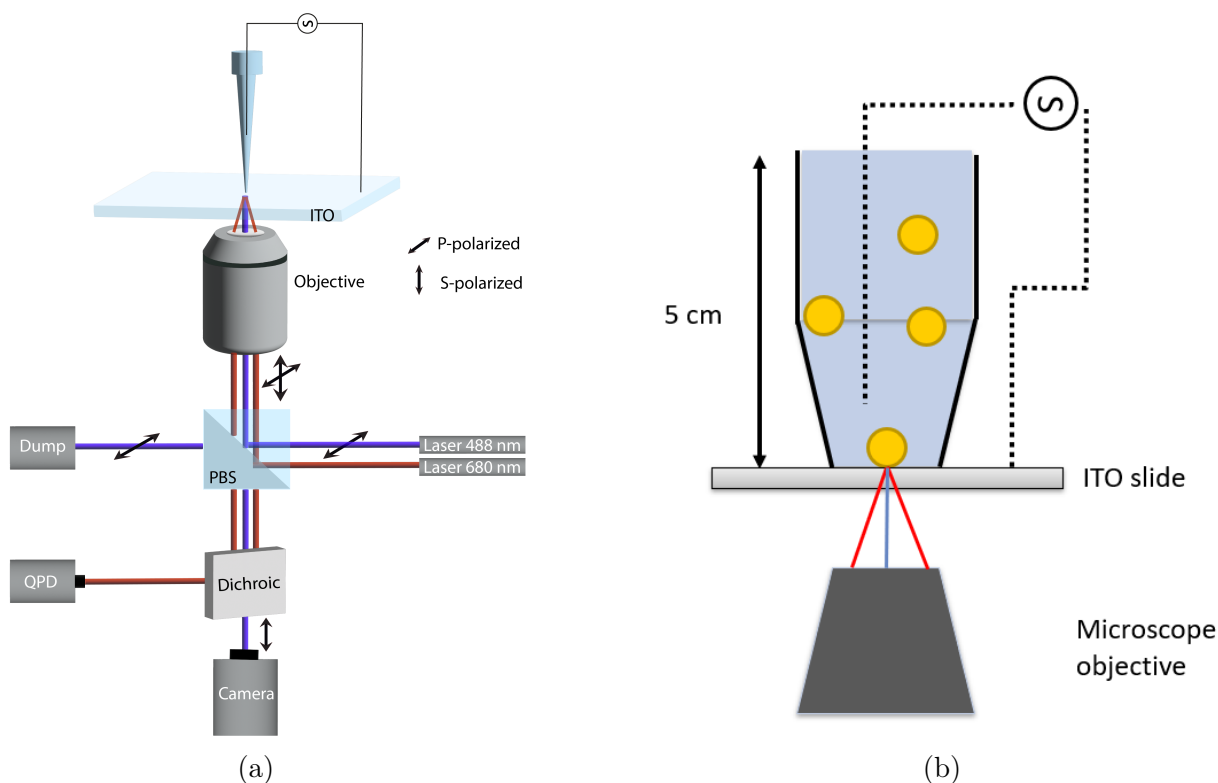


Figure 3.4: (a) Schematic of the dark-field microscope. From the blue 488 nm laser, p-polarized light enters the system and is split by a polarizing beamsplitter (PBS). The light propagates upwards through the objective and reaches the sample. The scattered light is now s-polarized and propagates to the camera. Meanwhile, the polarization of the red laser is not affected and reaches the sample under an angle. The reflected light propagates to a dichroic mirror, which points it to the quadrant photodiode (QPD) (b) Enlarged view of the ITO slide and pipette tip. The emulsion droplets (yellow circles) diffuse in the pipette and are constrained in their mobility. A top electrode wire is placed as close as possible to the ITO glass slide, without short-circuiting, represented with the dashed line.

Figure 3.5 illustrates the experimental DF-setup in which a pipette tip is placed on an conductive (ITO) bottom glass slide. The liquid inside the tip is illuminated with both the blue and the red laser light. From the topside of the tip, a conductive wire could be seen, which, together with the electrode pressing on the glass slide, forms a closed electronic circuit. This makes it possible to apply an electric field on the sample. An overview of the implemented electronic devices with their function is listed in subsection 3.3.3.

3.3.2 Software

Image recording on the DF-setup takes place using PyNTA exclusively, in which recorded signals are stored in HDF5 file format. The big advantages of PyNTA are the usability in samples with heterogeneous particle size and the easy-to-use graphical user interface. More details on PyNTA can be found in ref. [42].

3.3.3 Electronics and their function

The items listed below are used in the dark-field microscope setup.

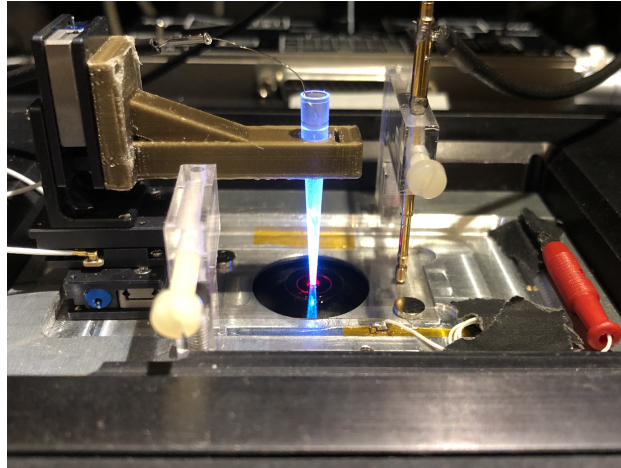


Figure 3.5: Photograph of part of the dark-field setup. The pipette containing the sample could be seen, as well as a thin top electrode wire bending out of the tip to the left.

- Blue laser light source (Coherent OBIS 488 nm LX): primary laser which illuminates the particle from below. The scattered waves are then collected.
- Red laser light source (Thorlabs CLD1010LP): secondary laser which also illuminates the particle, but incoming under an angle. Used to maintain focus during the experiment. Coupled to QPD and position detector.
- Oscilloscope (Keysight InfiniiVision DSOX2022A): visualizes the electronic signal during a measurement.
- Function generator (Hewlett Packard 33120A): gives input to the system, both frequency and amplitude. It provides a wave signal to the electrode of the measurement cell.
- Quadrant Photo Diode (QPD): collects the photons of the red laser, which are used for focus maintaining. This is coupled to the position sensing detector.
- Position sensing detector (Thorlabs Kinesis KPA101): enable automated alignment of red laser in closed-loop mode. This is coupled to the QPD.
- Current amplifier (Femto DHPA-100): transforms low input current to output voltage.
- Data Acquisition card (National Instruments USB-6216): acts as a readout mechanism of the different signals. Both optical (through current amplifier) and electronic signals are collected. The obtained signal is transferred through the DAQ and imported in further analysis software.
- Nano- and micro-drive C (MCL): these drives change the direction of the stage in all three dimensions; (z) with the nanodrive, (x, y) with the microdrive.
- Digital CMOS camera (Hamamatsu C11440): collects the scattered signal from the sample and transforms it to an image.

3.4 Simulation for background correction

As mentioned earlier in section 2.4, image analysis software could be used to characterize particles present in a measurement. To develop an accurate and sensitive method in detecting these particles, we first use a simulation that mimics particles as if they are landing in the camera frames. The part below describes the code that can simulate, visualise, locate and track particles, using background correction, intensity threshold and Fourier filtering. We start with an introduction into the essentials of background correction. Then, we continue with the various methods that are available and compare the results.

Introduction on landing simulation We focus on the adsorption (i.e., landing) of particles to a surface. We start with a theoretical simulation and after that use real-live data as input. By starting with a simulation, we can adjust many parameters of the system, such as particle size(-distribution), number and intensity and test different methods of background correction. Also other system variables, such as background noise, landing distribution and the field-of-view (FOV) could be changed. For the methods below, the background noise is increased and the extent to which particles could be detected correctly is tested.

We can define two goals in this simulation:

1. Subtract noise from the particle signal (background correction).
2. Correctly find and count the number of landed particles. This includes avoiding double counts & detection of particles that again leave from the surface (tracking).

The simulation is build up as a sequence of frames, each representing a FOV with particles appearing over time. Putting all frames behind each other, we have a movie dataset of a chosen length. We define the length by setting the number of frames (n_f) to a constant. The *seed* variable sets the random number generator and makes sure each simulation contains particles landing in the same order and at the same position. Therefore, the simulation is suitable to be used in the methods and compare the results directly.

In order to find all landed particles in a movie, one way to start is by selecting the last frame of the movie and then count the particles. Unfortunately, this does not take into account that particles can land very close together, causing them to be counted and detected as one, instead of two. Furthermore, in real data, particles can land and detach before the last frame is reached, again resulting in an incorrect particle count. Therefore, we need to find a way to count every particle, in every frame, while not counting background noise. The following parts all describe a specific method.

Method A: Applying a moving average

With this method, we subtract the *average* of the previous frame from the current frame. This not only works as a background correction, since constant noise over the frames is subtracted, but by doing so, particles that land consecutively, are counted individually. The number of frames to be subtracted could be chosen, e.g., subtract only the previous frame (1) or the average of the last x frames, where x is any arbitrary positive integer. If only one frame is subtracted, landed particles disappear after one frame in the correction. Subtracting 5 frames for instance makes more sense if a particle should be counted only when it has landed and remained stuck for a number of frames. Next, particles are counted in the background corrected frame. Also, a step-like function that shows the cumulative number of particles

as a function of the number of frames could be made based on the amount of particles in a frame.

When the noise is increased, this will eventually lead to false-positive counts, because any signal which matches the feature-finding parameters will be considered a particle. Therefore, only using a moving average will not suffice for data sets with (significant) noise.

Method B: Selecting an intensity cut-off value

A logic solution to the above problem of false positives is to apply an intensity cut-off at a certain point. This method acts as a brute force in doing background correction. For a frame, the corresponding intensity distribution is made. Next, an assumption is made that below a certain intensity value, only noise is present. In the histogram, it is determined where the noise ends and the signal starts, and all the low (noise) intensities are *cut-off* and put to zero. This is illustrated in Figure 3.6.

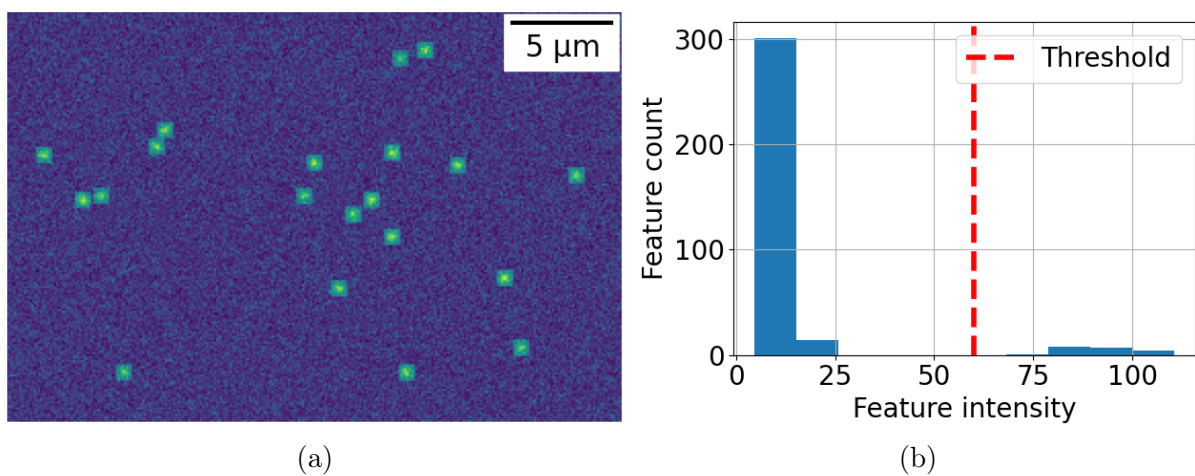


Figure 3.6: (a) simulated frame with 20 particles and background noise. (b) the resulting histogram of frame (a). The low intensity bars (≤ 40) are caused by the background noise, while the high intensity counts (≥ 60) are due to the simulated particles. The cut off threshold is set at $x=60$ in this case, as depicted with the red line.

Method C: Taking the fast Fourier transform

Besides applying an intensity cut-off, Fourier *filtering* could be used. It starts by transforming a frame with particles to Fourier space. Next, part of the frequencies are discarded: the high frequencies, which are mostly due to noise. The low frequencies are kept and inverse Fourier transformation is used to retrieve the original frame, but now without (most of the) noise present. The retrieved image is somewhat blurred, but still usable for particle detection using for example Trackpy. See Figure 3.7.

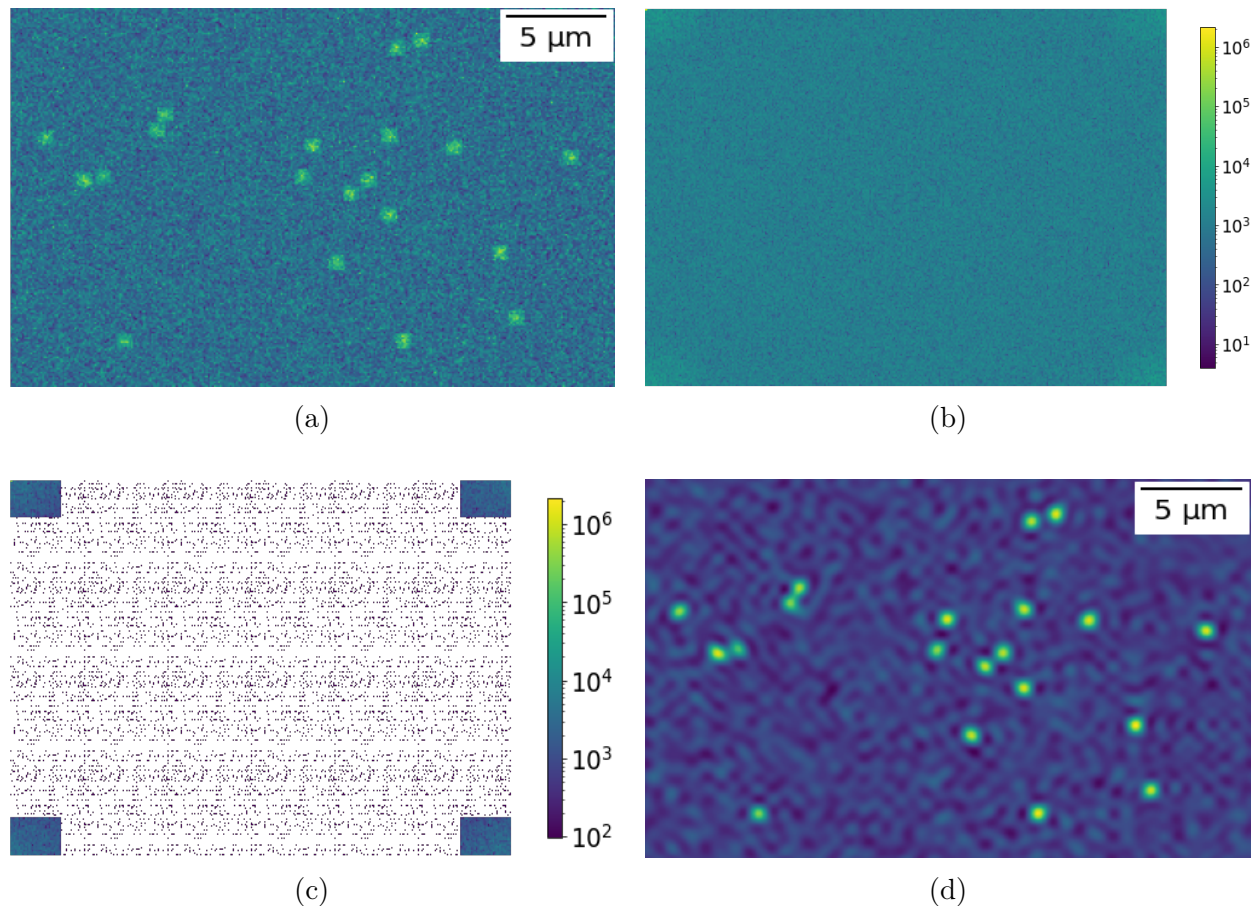


Figure 3.7: Process of using Fourier transformation to remove noise. (a) is a simulation frame and (b) is the Fourier transform of this whole image. Next, a fraction of the FFT is kept, denoted with the rectangles in (c). After an inverse FFT, plot (d) is obtained, showing the particles with less noise.

3.5 Particle scattering simulation: in- and output

In this part, another simulation is discussed, namely SMUTHI. This numerical method could calculate the scattering of particles with different shapes and sizes. Every SMUTHI scattering simulation is build up in three parts:

1. Initialising the layer system. Objects are placed at a specified position in the layer system. As first layer, a substrate is chosen (e.g., glass). Secondly, an layer such as water is added, in which one or more particles could be placed. On the interface of this two-layer system, the coordinate system is chosen such that this point is defined as $z = 0$. The thickness and refractive index of the material are selected. By adding a third layer, the glass flow channel could be mimicked.
2. Initial propagation field. Options include a plane wave, a Gaussian beam and dipole sources. For our purpose, we focus on the plane wave and select: wavelength in vacuum, polar angle, polarization, azimuthal angle. Although we illuminate our sample with polychromatic (i.e., white) light, we have to select a single wavelength. A wavelength of 550 nm has been chosen, for this is at the top of the spectral response of the camera and in the middle of the visible light spectrum. The polar angle represents the propagation

direction of the k -vector, with 0 meaning parallel to the z -axis. Closely related is the azimuthal angle, which defines in which plane the k -vector propagates. In this case, 0 means the k -vector is in the x - z plane. The polarization value determines the electric field vector direction and can be either 0 or 1, representing transverse electric (s) or transverse magnetic (p) polarized light, respectively.

3. Particles. Spherical particles are used and the radius, refractive index and the position in the layer system is chosen.

With these three parts defined, we can run the simulation and process the data. As output, several options exist, which are listed below:

- Near field gives the electric field distribution as a function of position. The distribution can be visualised by generating a plot.
- Far field gives the intensity distribution in direction space, far away from the scattering source.
- Cross section calculation, as discussed earlier in subsection 2.2.2.

For the scattering profiles, Figure 3.8 illustrates the relevant wave propagation directions, based on a two-layer system.

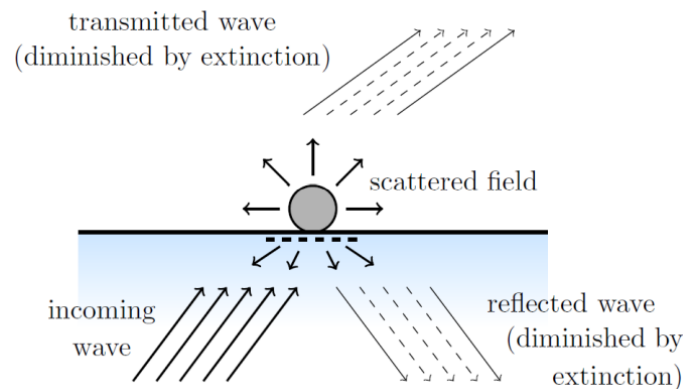


Figure 3.8: Schematic illustration of the different types of waves present in the simulation. The black dashed horizontal line represents the image plane position (i.e., the position of the focal point). This collects the scattering signal which propagates in that direction. Reprinted with permission from ref. [40]. Copyright 2022 Elsevier.

Chapter 4

Results and discussion

This chapter starts with the results of the landing simulation and related trackpy scripts. Then, the first experimental steps with flow channels and the preparation of the samples is discussed. This is followed by the characterization of polystyrene and the size determination of the oil-in-water emulsions, including a comparison with a numerical simulation. Lastly, the results from the dark-field microscope involving the application of an electric field and subsequent frequency response are reported.

4.1 Particle landing simulation and data processing

As mentioned earlier in section 3.4, a simulation is used to mimic the landing of particles on a surface, of which an example is displayed in Figure 4.1a. Such a frame is then used to count the particles, and various methods are tested with the goals of decreasing background noise as much as possible, and avoid counting duplicates that may lead to wrong particle detection. In the following parts, the three methods (moving average, threshold and FFT) are discussed.

4.1.1 Moving average and cumulative landing

The moving average method subtracts the mean of the previous frame from the current frame, and does so for every frame in the simulated series. As a result, landed particles stand out more against the noisy background, which makes counting more reliable. The simulation started with a fixed amount of particles and frames. As a result, by counting for each consecutive frame the amount of particles that appear in each frame, it is possible to construct a cumulative landing plot, as displayed in Figure 4.1b. This plot shows the random order in which the particles land over time, using the moving average method.

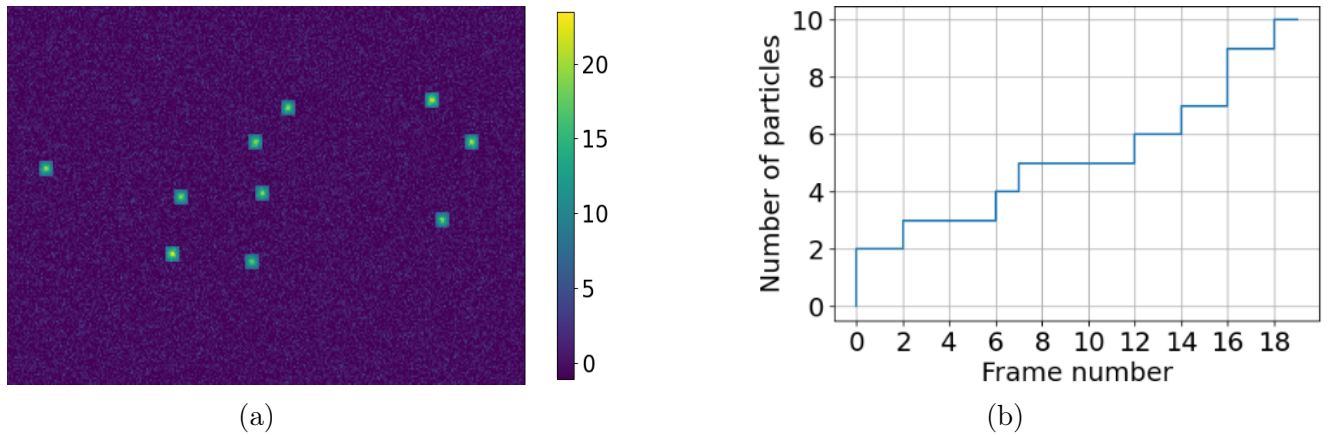


Figure 4.1: (a) Simulated frame in which some particles have landed (yellowish spots), using the moving average method. The color bar represents the pixel intensity. (b) Particles are located and counted using trackpy, and the cumulative particle counts is plotted during the course of the simulation. Note that the moving average takes one frame off from the started amount (19 instead of 20) and that two particles land between frame 0 and frame 1, resulting in the value at frame 0.

To continue with the effect of background noise on the detection of particles, different levels of background noise have been applied on the simulation with the same parameters; only the background noise has changed. Using the moving average, the last frame of the simulation, as well as the results from trackpy on that frame, are displayed in Figure 4.2.

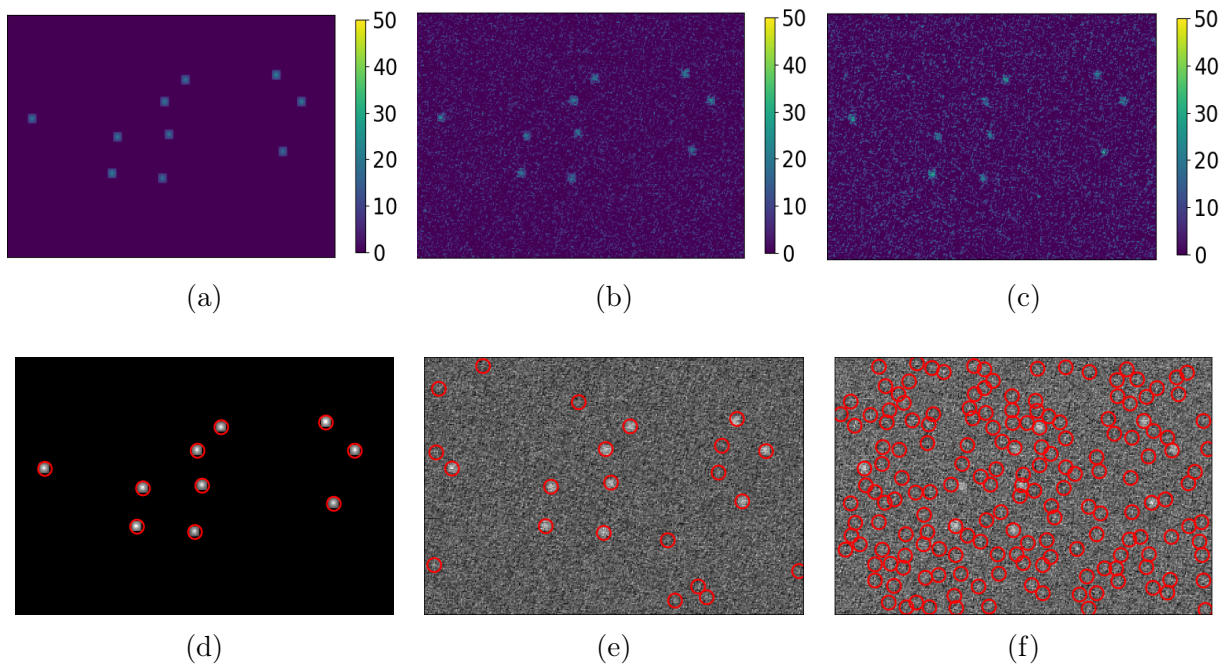


Figure 4.2: (a - c) Simulated frame with noise = 0, 20 and 40, using the moving average. (d - f) Trackpy particle locating on the simulated frames. Without any noise present (a), all particles are counted, whereas noise values of 20 (e) and 40 (f) result in a too high particle count, in which some of the noisy pixels are considered a particle.

Next, the noise value in the simulation is changed in small steps ($0 \rightarrow 20$) and the detected features are counted. In this way, the point is determined at which the moving

average output crosses the ground truth (i.e., the real number of particles). The used noise value is divided by the simulated particle intensity, resulting in a noise-to-signal ratio. From this point onward, the noise-to-signal ratio is abbreviated as NSR. The NSR will be used to compare the different methods in terms of usability in detecting “true” particles from noise.

From Figure 4.3, it could be seen that up to a $\text{NSR} = 0.37$, the moving average is capable of retrieving the correct amount of particles. Higher noise values will lead to false positive counts.

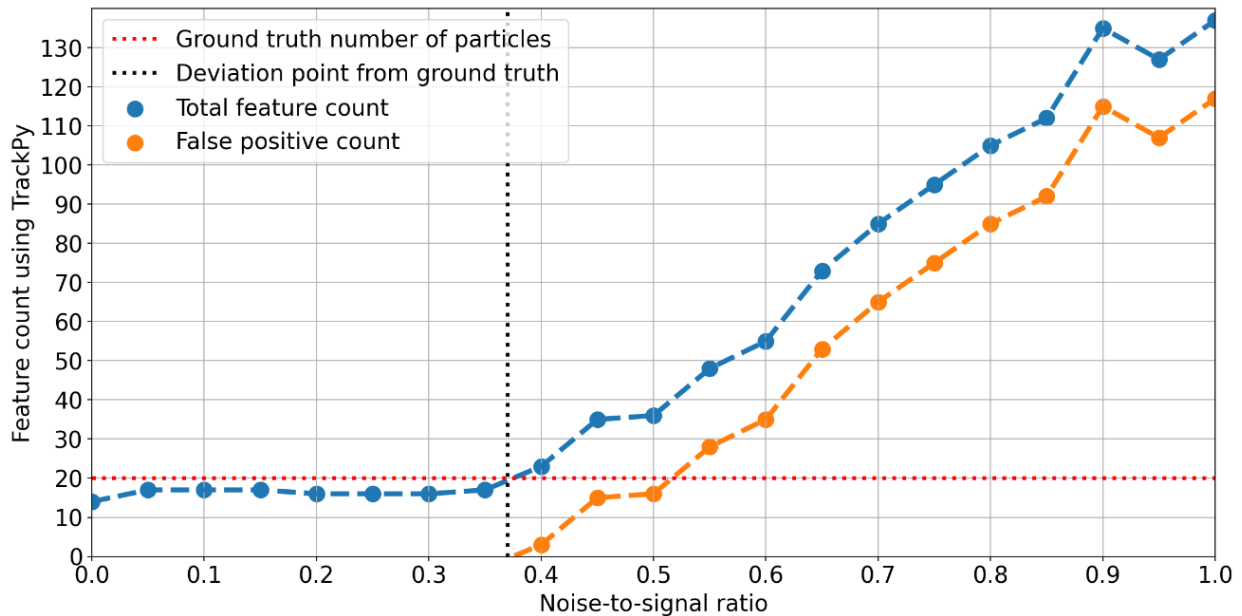


Figure 4.3: Locating simulated particles for different levels of noise using the moving average method. The ground truth (i.e., real number of simulated particles) is displayed with the dashed red line. The vertical dashed line shows the noise-to-signal value at which the moving average no longer only finds the correct amount of particles, but also false positives are counted.

4.1.2 Intensity cut-off

The frame-by-frame subtraction in the moving average cannot differentiate anymore from a certain noise value, so we continue with another method, namely applying a threshold. This method uses the intensity distribution in a histogram of the simulated frame. By visually inspecting the histogram bars from the simulated frame, it is possible to select a cut-off value, at which the low intensity noise speckles are discarded, while keeping the high-intensity “real” particles. This value is called the cut-off threshold and this principle is displayed in Figure 4.4.

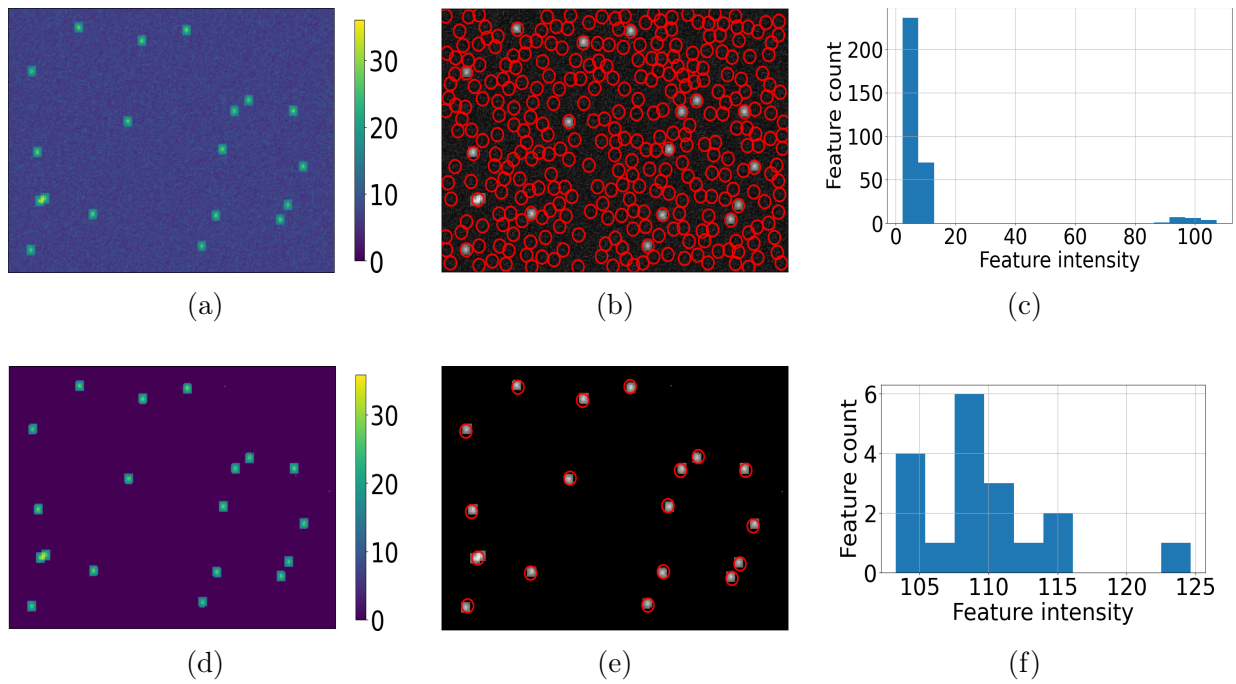


Figure 4.4: Threshold determination to remove noise from the background. (a) represents the simulated frames before applying a cut-off, in which a noise value = 1 is used. (b) Using trackpy locate on (a) results in a too high feature counts, as can be seen with the many red circles. (c) the resulting intensity distribution of the located features in (b). Noise features (intensity ≤ 20) and particle features (intensity ≥ 70). Selecting a cut-off threshold at intensity = 50 in (c), results in the figures (d - f). Note that the background noise is reduced, when panel (a) and (d) are compared. (e) The correct amount of particles is detected.

In the same way as with the moving average method, to test the limitations of applying an intensity threshold, different noise values in the simulation are applied and the located feature count is compared to the ground truth. Figure 4.5 shows the number of counted particles versus the noise value in the simulation. Since a single cut-off value will not suffice for either a low noise value, or a high one, the cut-off value increases along the increase in noise value.

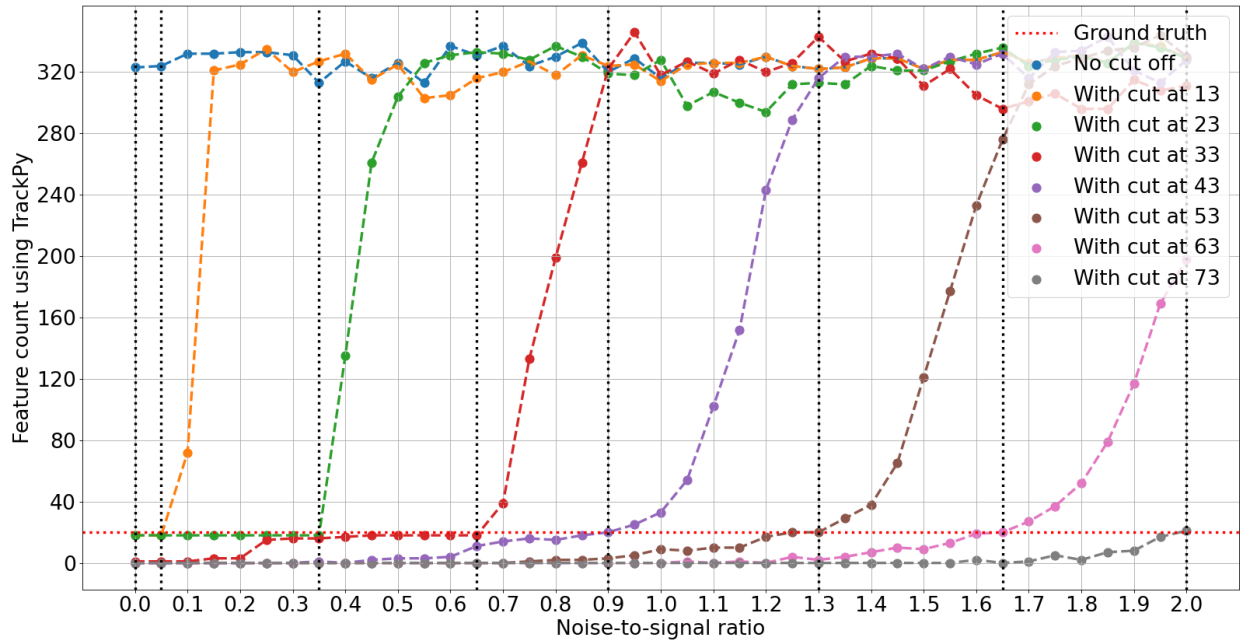


Figure 4.5: Locating simulated particles for different levels of noise and cut off values. The ground truth (real number of simulated particles) is displayed with the dashed red line. The vertical dashed black lines show the noise value at which that cut off value causes a deviation in the number of located particles, compared to the ground truth. For a cut off value of 23 for instance (green line), the correct amount of particles is returned for an NSR between 0 and 0.35, after which it starts deviating. Increasing the cut off value will shift this deviation point to larger noise values.

From Figure 4.5, it can be concluded that, dependent on the cut off value, the correct amount of particles could be retrieved, up to at least a NSR of 2. However, this method thus requires a increasing cut-off threshold for each individual measurement. If the experimental conditions allow, this might not be a problem, but we continue with a third and final route, which could be used regardless of the noise value.

4.1.3 Fourier filtering

As shown in section 3.4, using Fourier filtering could make the simulated particles stand out more against the background (noise), by filtering out these high-frequency noise features. Again, different noise values were used in the simulation and the retrieved particle count was plotted against the NSR, as displayed in Figure 4.6. Also, for comparison, the results of only using trackpy locate, so without any other procedure, such as moving average, are also displayed as a function of NSR.

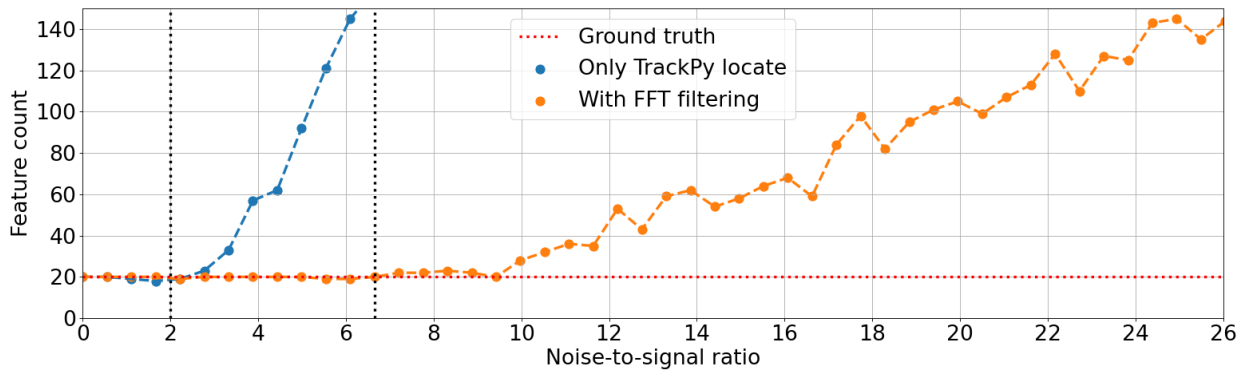


Figure 4.6: Locating simulated particles for different levels of noise using Fourier filtering. The ground truth (i.e., real number of simulated particles) is displayed with the dashed red line. Both the results from the trackpy locate function (blue) and Fourier filtering (orange) are shown. The vertical dashed black line (at $\text{NSR} = 2$) shows the noise value at which a deviation in the number of located particles occurs, using the trackpy locate function exclusively. The second vertical dashed line (at $\text{NSR} = 6.5$) shows this point using Fourier filtering.

From Figure 4.6, it could be seen that the Fourier filtering works well in retrieving particles up to relatively high NSRs (up to 6.5). Compared to the previous two methods, moving average and cut-off threshold, Fourier filtering works for the highest noise values, and, dependent on the available dataset and experimental conditions, might be the first choice. However, Fourier filtering requires some more computational steps, compared to background subtraction and intensity cut-off.

4.2 Experimental measurement preparation

From the investigation of different methods to reduce background noise in simulations, we continue with a description of the experimental preparation steps. First, we go into the preparation of a flow channel, after which polystyrene particles are diluted and imaged. This section ends with the preparation of the used emulsions.

4.2.1 Flow channel properties

Several flow channels are constructed, using different materials to connect the two glass slides. In thickness varying double-sided tape is used to attach the bottom glass slide to the cover glass slide. With a dilution containing polystyrene particles, an estimate is made of the thickness of this flow channel. By changing the focal point of the objective, the particles appear out-of-focus, in focus and out-of-focus, respectively. In the bright-field microscope, this is employed by starting with the focal point below the bottom glass slide, after which the objective is moved upwards, resulting in the focal point advancing through the flow channel, and ending at the cover glass slide. Since the coarse adjuster used to move the stage contains numerical divisions, it is possible to determine the distance the stage has moved.

By changing the coarse adjuster, images were taken of particles appearing out-of-focus, then in focus, and eventually out-of-focus again, which is displayed in Figure 4.7. After converting the units on the adjuster to actual distances, this resulted in a thickness of $25\ \mu\text{m}$. Aiming for the smallest possible channel thickness will help in identifying single

particles, because the changes of overlapping particles decrease, and the used scattering simulation package cannot cover larger layer systems. Parafilm could be made such that it is significantly smaller compared to other double-sided tapes available (75 μm and 260 μm , based on the manufactures specifications).

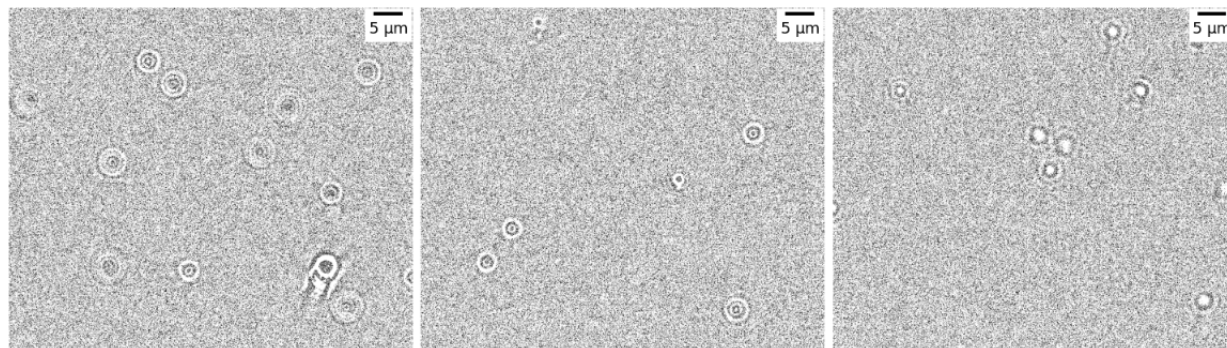


Figure 4.7: By varying the position of the objective, while keeping the sample fixed, a z-scan through the flow channel is made. As a result, the thickness of the flow channel could be estimated; here: 25 μm . The material used to connect the glass slides was parafilm. It was heated and stretched to obtain a thin slab.

4.2.2 Diluting polystyrene particles

From the flow channel preparation, we continue with the search for an optimum concentration for single-particle imaging. Starting from the purchased (concentrated) polystyrene bottle, multiple dilutions were prepared using deionized water. Once a dilution was made, bright-field microscopy was used to image the concentration; if the concentration was too high, further dilutions were made. Trial-and-error resulted in a starting dilution of 10^4 , required to count single particles. Further dilutions (up to 10^5) were made and the particles were counted. By changing the (2D) position of the imaged flow channel regions, different parts of the flow channel were imaged to reduce the change of imaging a region with too much/little particle. In this way, a representative particle distribution could be obtained. The resulting counting is plotted against the dilution and displayed in Figure 4.8.

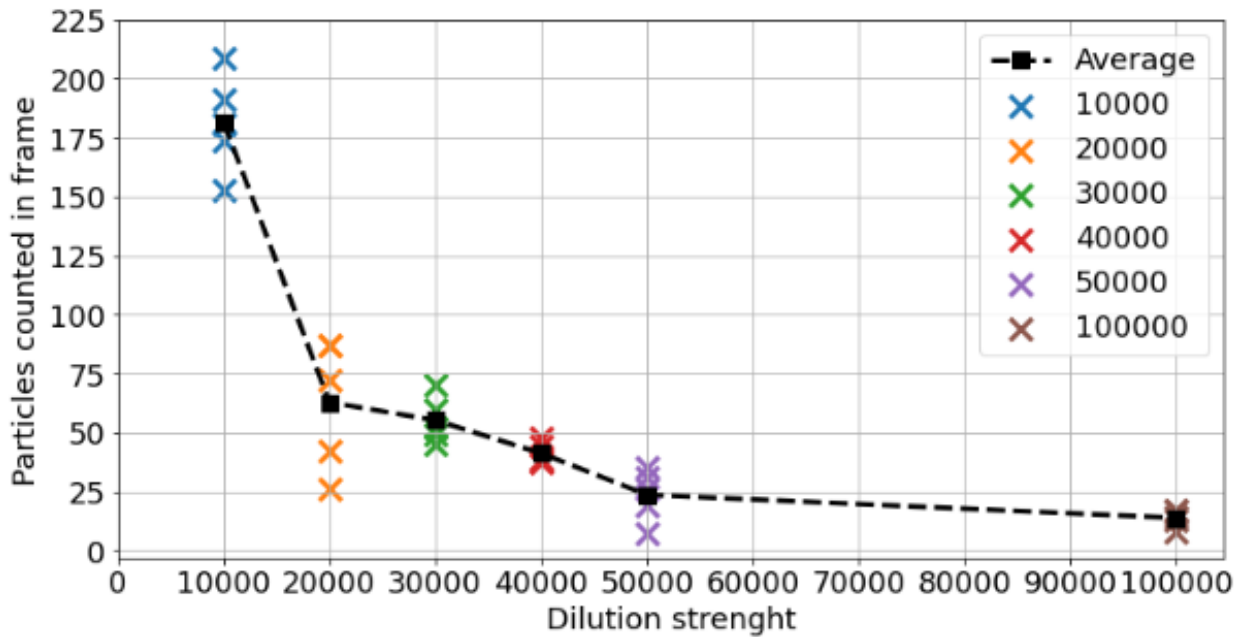


Figure 4.8: Diluting 300 nm polystyrene particles in deionized water. The y-values represent the number of single particles counted in a frame, using trackpy. For each dilution, five separate frames were selected, displayed with the cross marks, and the averages are connected with the black line. The x-axis shows the dilution strength, where 10,000 means a dilution of 1:10,000.

4.2.3 Emulsion preparation

Besides the predefined polystyrene particles, also emulsion droplets are used in this work, with, a priori, an unknown particle size. By adding and shaking oil and water, an oil-in-water emulsion was formed. Addition of an emulsifier made the formed emulsion less unstable. Here, octane (as oil), deionized water and polysorbate-20 (as emulsifier) were mixed to form an emulsion, as displayed in Figure 4.9.

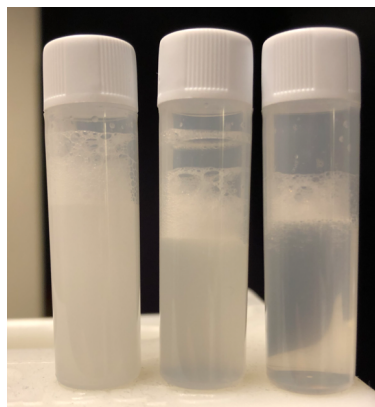


Figure 4.9: Oil-in-water emulsion formed by mixing octane, deionized water and polysorbate-20. The three bottles represent the as prepared solution (left) and the 1:10 and 1:100 dilutions (middle and right, respectively). Since the bottles are capped, the foam cannot evaporate quickly and remains on top.

4.3 Size measurement in the bright-field microscope

Now the preparations are discussed, we continue with the size determination of the prepared emulsions. Size we use the scattered particle intensity as a measure for the particle size, we first need some intensity values for well-defined particle sizes. For this, several polystyrene particles with different sizes were used, as shown in the next part. After that, we take a short look at the size-dependence in scattering, namely the extinction efficiencies using numerical simulations. The last part will cover the size determination of the emulsion particles.

4.3.1 Characterization of pre-defined particles

Polystyrene particles ranging between 100 nm and 3 μm were diluted to single-particle concentration. Then, an image with single-particles visible was taken with the bright-field microscope, and with the trackpy locate function, an intensity value was obtained, for this specific particle size. This procedure was repeated for different sizes, and the resulting intensity vs particle size was obtained, as displayed in Figure 4.10.

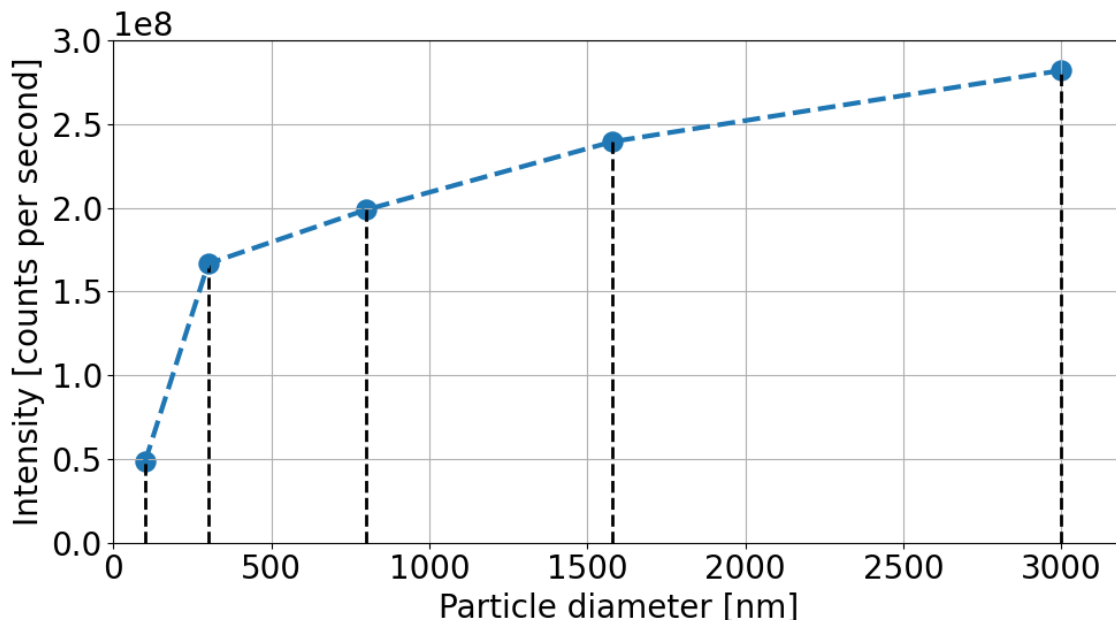


Figure 4.10: Intensity versus particle size of purchased polystyrene particles, diluted in deionized water. The camera exposure time was equal to 15 ms and used to convert arbitrary intensity units to counts.

4.3.2 Comparison with numerical simulation

The shape of the plot in Figure 4.10 shows the relation between particle size and scattered intensity for this type of particle. With numerical simulations of the extinction efficiency, which denotes the portion of the incident plane wave that is affected by the particle, relative to the cross sectional area of the particle. For two numerical packages, SMUTHI and Miepython, this extinction efficiency is calculated, as displayed in Figure 4.11.

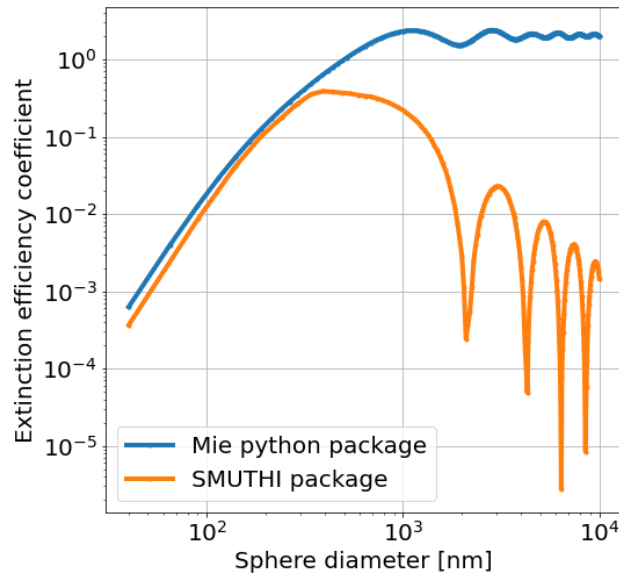


Figure 4.11: Scattering efficiency calculation with SMUTHI and Miepython for different sizes. When the particle size equals the illumination wavelength, SMUTHI starts to show a decrease in the coefficient. This could be explained, because the illumination is the same for all cases, whereas the geometric cross section increases, leading to a smaller scattering coefficient. The used script is taken up in section B.1.

In experiments, an increasing particle size will not lead to the sharp decrease as shown by SMUTHI in Figure 4.11. The “peaks” occurring at particle sizes $\geq 10^3$ originate from Mie resonances, certain sizes that scatter remarkably stronger.

To take a closer look at the accuracy of the SMUTHI calculation, that parameter that describes the sphere is investigated. In SMUTHI, the particle description depends on the complexity of the used multipole degree, L_{max} . This value displays the amount of spherical wave expansions used to describe the incoming and scattered field. As can be seen in Figure 4.12c, an increase of the used multipole degree changes the scattering efficiency coefficient. In general, larger L_{max} leads to a more accurate calculation, albeit at an increased computational cost.

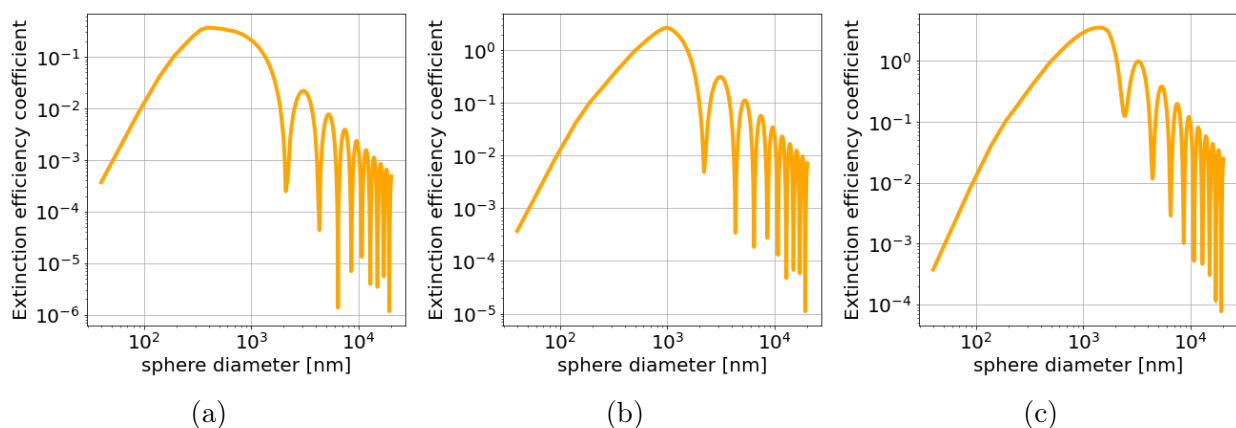


Figure 4.12: Changing the used multipole degree from one (a) to six (b) and 12 (c), in SMUTHI. A larger multipole degree will lead to larger scattering efficiencies, especially at larger sphere sizes. The used script is displayed in section B.2.

4.3.3 Characterization of emulsion particles

From the polystyrene particle characterization and a sidestep into related numerical simulations, we continue with the size determination of the prepared emulsions. The 1:10 diluted oil-in-water emulsion (from Figure 4.9) was added to a 75 μm thick flow channel, using double-sided tape. By changing the focal point, the objective was set such that a focused image of the particles could be obtained, as displayed in Figure 4.13.

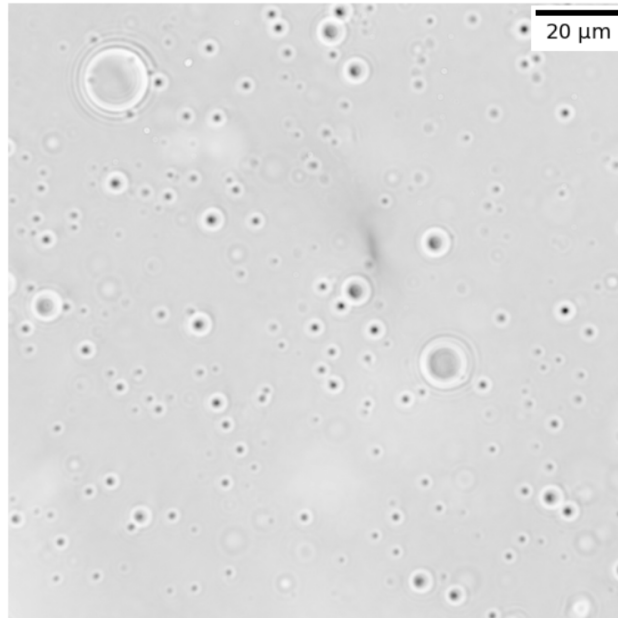


Figure 4.13: Bright-field microscope image of a 1:10 diluted oil-in-water emulsion. The pixel values are inverted for clarity, leading to dark (in focus) droplets. Also note the polydispersity in size.

From this image, by using the `trackpy` `locate` function, it is possible to get an intensity distribution. Instead of using only one frame to get an intensity value, a whole series of images is taken for 30 to 60 seconds measurement time to get a reliable estimate of the mean intensity. This measurement used the background subtraction option in `PyNTA`, in which an similar flow channel was used as reference. Then, without changing the focus, the sample was introduced and the recording took place. As the emulsion droplets diffuse over time, sometimes particles are in the focal plane, and sometimes a blur or fringe pattern is observed. All particles appearing in the focus plane are analysed via counting and tracking using `trackpy`. The results are shown in Figure 4.14. Again, arbitrary intensities are divided by the camera exposure time.

The histogram showing the relative particle intensity is normalized, meaning the area under the histogram will sum to 1, using the density function in `matplotlib`*.

*Histogram normalization using the `density` keyword in python.

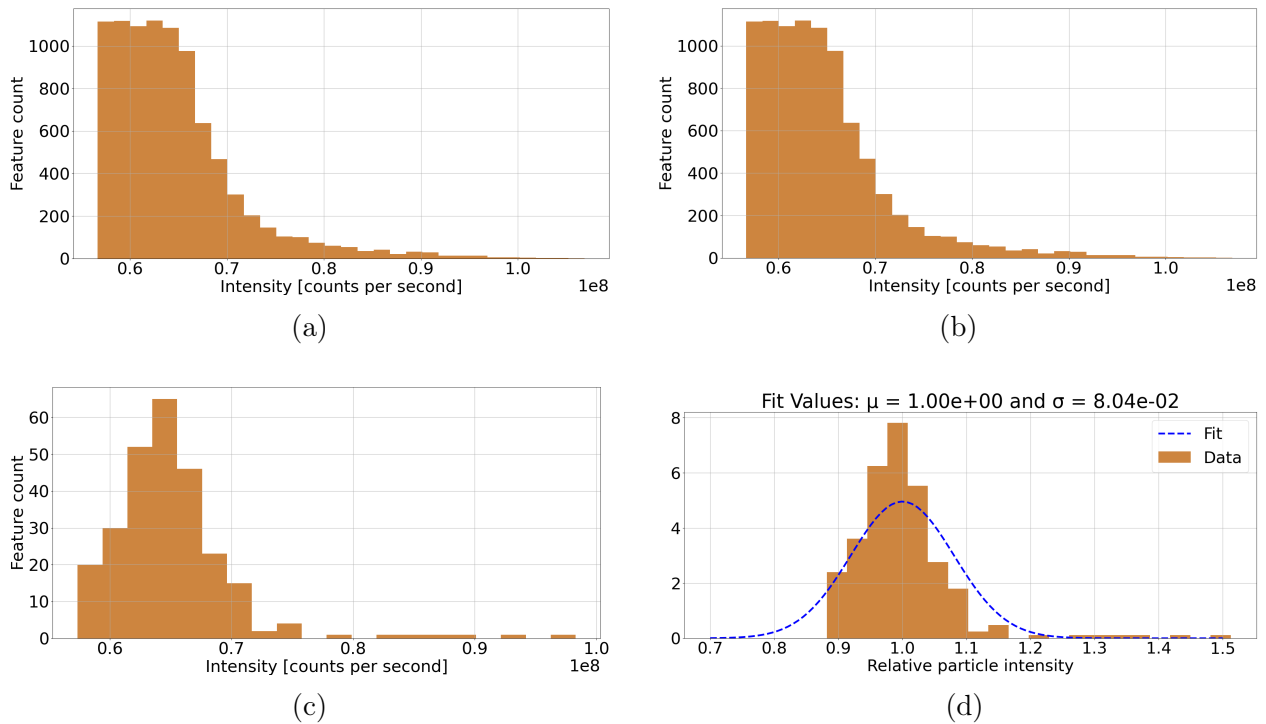


Figure 4.14: Image processing using trackpy on a series of frames containing oil-in-water emulsion droplets. (a) Any bright spot is located in every image. (b) Using frame-by-frame comparison, trackpy links the same particles. (c) Removal of spurious features (i.e., only in focus plane for one or two frames) leads to a clear decrease in feature count. (d) Dividing the mean intensity from (c) will give a relative particle intensity distribution. Fitting this with a normal (Gaussian) distribution gives the mean (here: 1, due to the relative intensity) and standard deviation, as shown in the plot title.

At this point, the mean intensity of the emulsion droplets is converted into a size distribution using the previously determined intensity-size relationship with polystyrene particles, since both experiments take place on the same microscope. Also, the same flow channel thickness is used, with the same focal point and image software (PyNTA). The mean particle intensity of $6.5e+07$ from Figure 4.14c, corresponds to a size of ≈ 128 nm in Figure 4.10. After transforming the intensity values to sizes, the particle size distribution of the oil-in-water emulsion could be calculated, as displayed in Figure 4.15. Again, a normal distribution fit was used to get the mean and standard deviation, leading to 128 ± 10 nm.

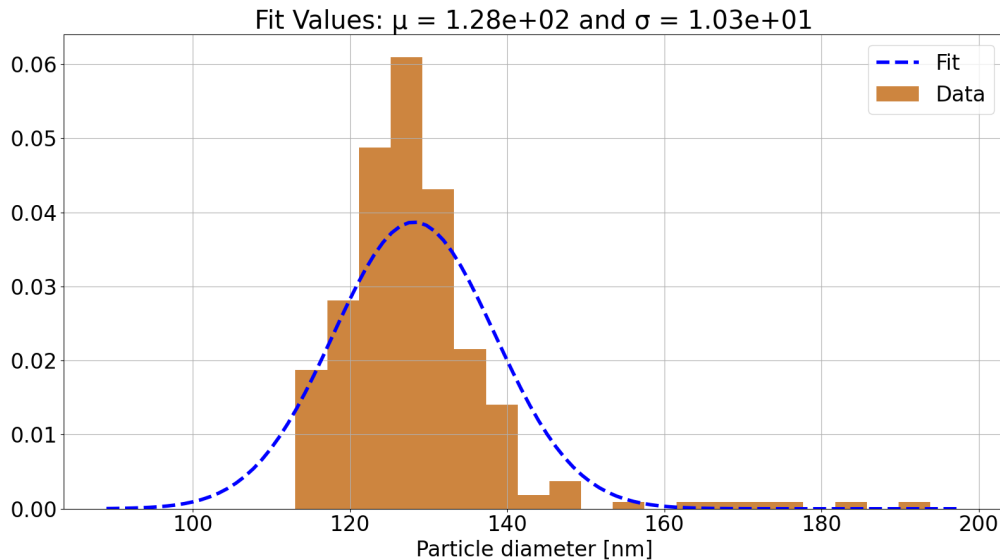


Figure 4.15: Calculated particle size distribution of the prepared oil-in-water emulsion. The mean value and standard deviation are shown in the plot title. The histogram is normalised, showing a probability density on the y-axis.

Note that two assumptions are made with respect to transforming the intensity as size measurement, namely:

1. The polystyrene particles scatter in the same way as the created oil-in-water emulsion. Although the polystyrene particles are diluted in water, and water is the external phase of the emulsion droplet, the refractive indices of polystyrene (1.5916) and octane (1.3989) differ, potentially leading to a difference in scattering signal.
2. The sharp increase in the low-size regime of the polystyrene particles, makes that a small change in mean emulsion intensity has a great effect on the calculated particle size distribution. Having polystyrene particles with a smaller difference in size, such as $50 \rightarrow 300$ nm in steps of for example 50 nm would help in getting a more accurate intensity-size relationship.

4.4 Experimental and simulated scattering patterns

Now that the size of the emulsion particles has been estimated, we continue with an examination of the observed scattering pattern. Note that particles in focus give a circle as center point, whereas particles out-of-focus give a fringe pattern or a blur, dependent on their position w.r.t. the focal point. Characterization of this scattering profile might give information on the particle position in the medium (i.e., flow channel).

First, the outcomes of a numerical simulation are discussed, after which an experimental scattering pattern is investigated.

4.4.1 Changing particle position in SMUTHI

As mentioned in subsection 2.4.4, SMUTHI could be used to generate the scattering electric field profiles of a single particle in a custom layer system. Since our experimental flow channel could be compared with such a theoretical layer system, SMUTHI was used. In one of the simulations, the scattering profile was simulated for a varying particle position, while keeping the image plane fixed. Initially, the particle was positioned close to the bottom glass surface, and with a certain step size, this position was changed to be more near the center of the flow channel. The following parameters were used: flow channel thickness = $15\ \mu\text{m}$, particle diameter = $400\ \text{nm}$ and a fixed image plane position of $-100\ \text{nm}$, so below the the (bottom) interface layer. Varying the particle position will change the scattering pattern, as displayed in Figure 4.16.

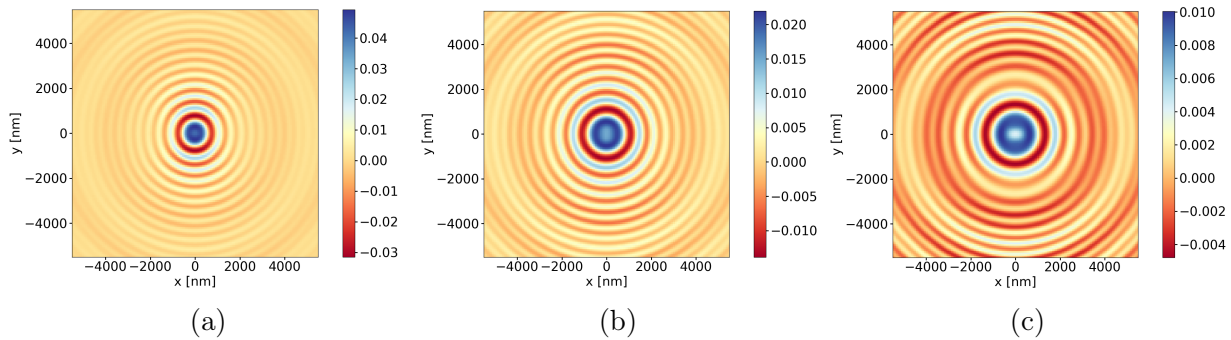


Figure 4.16: Simulated scattering electric field profile for a $400\ \text{nm}$ spherical particle. The particle is positioned at (a) $1\ \mu\text{m}$, (b) $2\ \mu\text{m}$ and (c) $3\ \mu\text{m}$ from the bottom of the $15\ \mu\text{m}$ thick flow channel. The color bar represents the electric field values, and a clear fringe pattern could be observed by the many rings. The used script could be found in section B.3.

The electric field pattern could be squared to obtain the intensity. Since the source produces a radially symmetric pattern, the *radial average* could be calculated. This pattern would show the transition between the interference fringes as peaks. Since the (simulated) scattered intensity depends on the particle position, investigation of this pattern could be used to identify the position of particles in an experimental setting. To do so, the periodicity of the radial averaged signal could be Fourier transformed, resulting in a frequency spectrum of the oscillatory scattering pattern. Besides the amplitude (i.e., magnitude after FT), the phase angle (at peak frequency) of the signal could be calculated. An overview of this procedure, starting from simulated field and leading to the phase angle, is shown in Figure 4.17.

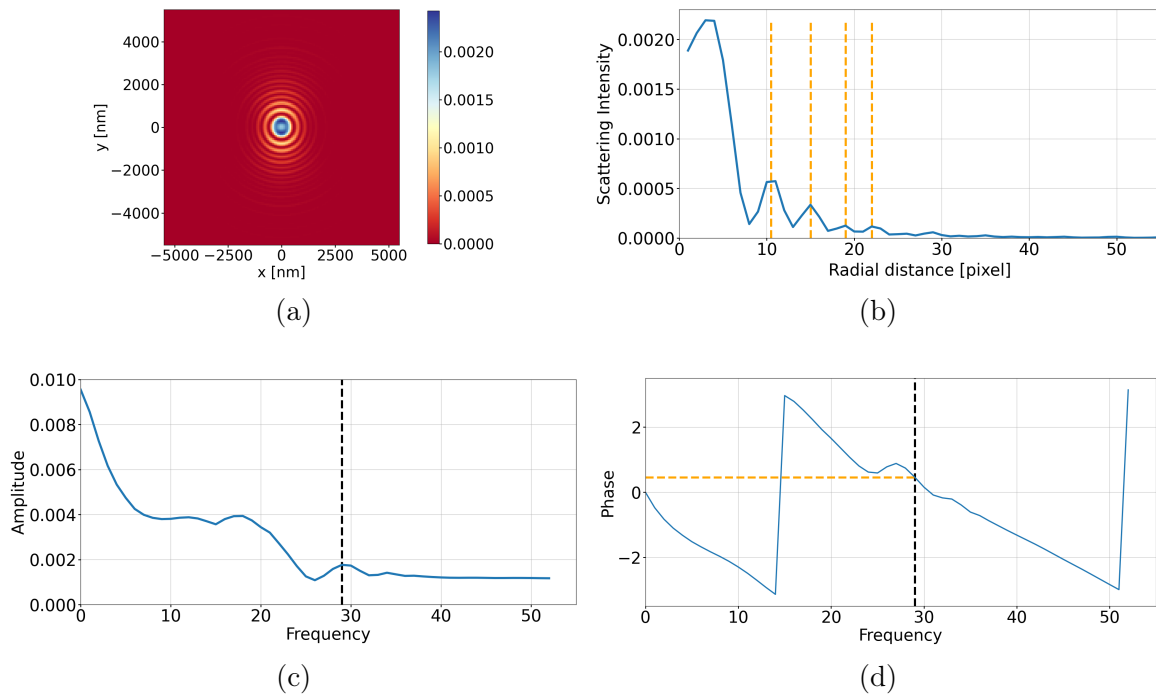


Figure 4.17: Phase retrieval of a simulated, oscillatory scattering profile, using SMUTHI. (a) The electric field is squared to obtain the intensity. The color bar denotes the scattered intensity. (b) The radial averaged plot of the intensity pattern from (a). (c) After taking the fast Fourier transform, a frequency spectrum is obtained. The highest frequency peak is selected (black dashed line). (d) Phase angle is calculated after Fourier transformation of (b). The peak frequency is illustrated with the black line. The corresponding phase is shown as the orange line.

This process is then repeated for different particle positions in the layer system, and the calculated phase values for these positions are shown in Figure 4.18.

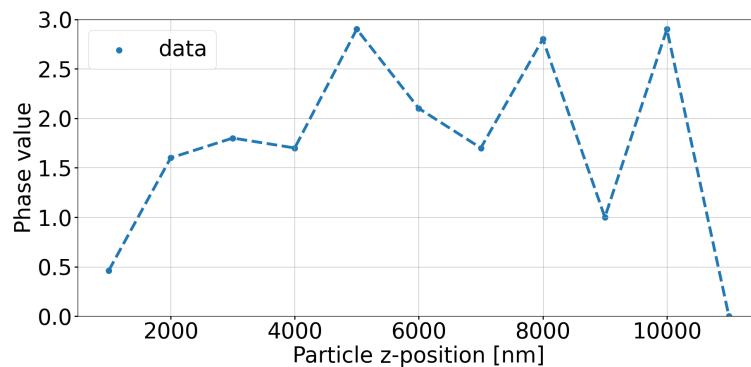


Figure 4.18: Overview of the phase values obtained at the peak frequency, after Fourier transformation of the radial intensity average. The x-value shows the particle's position in the simulated layer system.

4.4.2 Experimental particle scattering pattern

Next to using a simulated scattering profile, an experimental image is used, in which a fringe pattern is observed. The pattern of a 300 nm polystyrene particle dispersed in water is analysed in the same way as the simulated patterns. The results are shown in Figure 4.19.

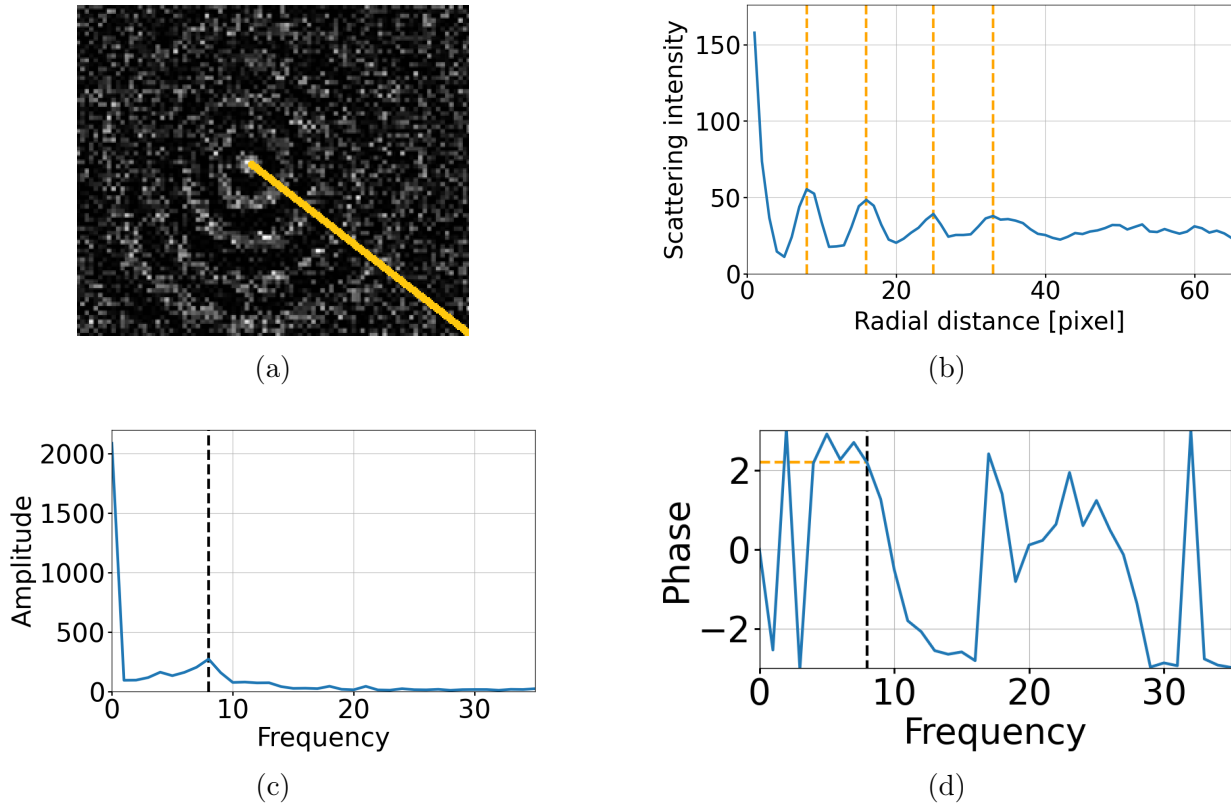


Figure 4.19: Phase calculation of an experimental fringe pattern. (a) An image of a polystyrene particle showing 4 rings is taken with the bright-field microscope. The yellow line denotes the path of the radial average, resulting in panel (b). (b) The radial average of the fringe pattern in (a). (c) After taking the Fourier transform, a frequency spectrum is obtained, in which the peak frequency is shown with the black vertical line. (d) From the Fourier transform, the phase is calculated and plotted. At the peak frequency (black line), the corresponding phase is indicated (orange line).

Comparing the phase of such a fringe pattern, both simulated and experimental, has some important considerations, including:

1. The Fourier transformation does not suite the available data from the scattering that well. Perhaps a different function that calculates the periodicity of the radial averaging plot or fringe pattern could be useful. A Hankel transformation was tried, but turned out unsuccessful.
2. To make a direct comparison between experimental phase and simulated phase, the parameters for the simulation should correspond to the experimental (flow channel) parameter, or vice versa. Here, the simulated layer system thickness (15 μm) and particle size (400 nm) do not fully correspond to the experiment (75 μm thickness and 300 nm size).

Once these issues are resolved, it could be interesting to relate the experimental pattern to the simulated one and in that way, characterize a particle with high accuracy.

4.5 Characterization on the dark-field microscope

So far, the particle size has been determined for an oil-in-water emulsion and further characterizations have taken place. We now change to the second part of the title of this thesis, namely the part on “frequency response”. This requires a few changes, namely we only consider emulsion droplets (no polystyrene), the use of the cross-polarization dark-field microscope (rather than the bright-field microscope) and the implementation of particle actuation through an electric field (instead of size determination).

4.5.1 Emulsion visualisation

With the dark-field microscope, both oil-in-water and water-in-oil emulsions have been investigated. Figure 4.20 shows an image of two oil-in-water emulsion droplets. The characteristic clover leaf structure, due to cross-polarization, is visible.

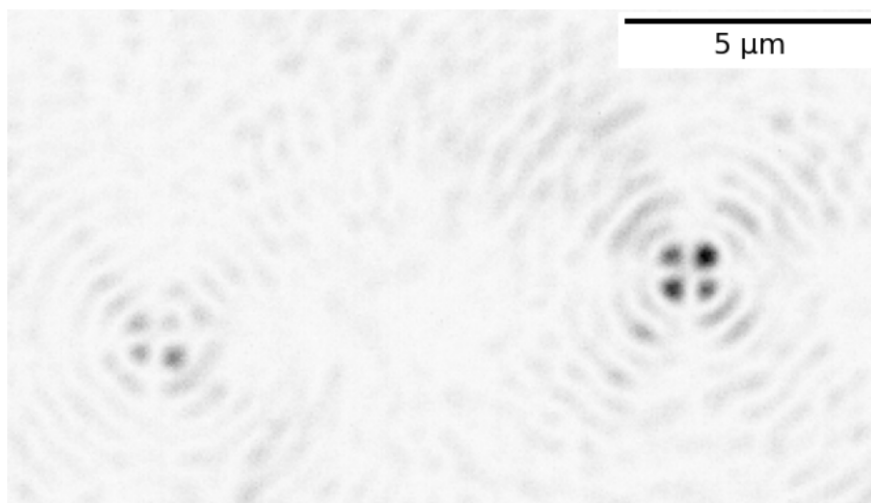


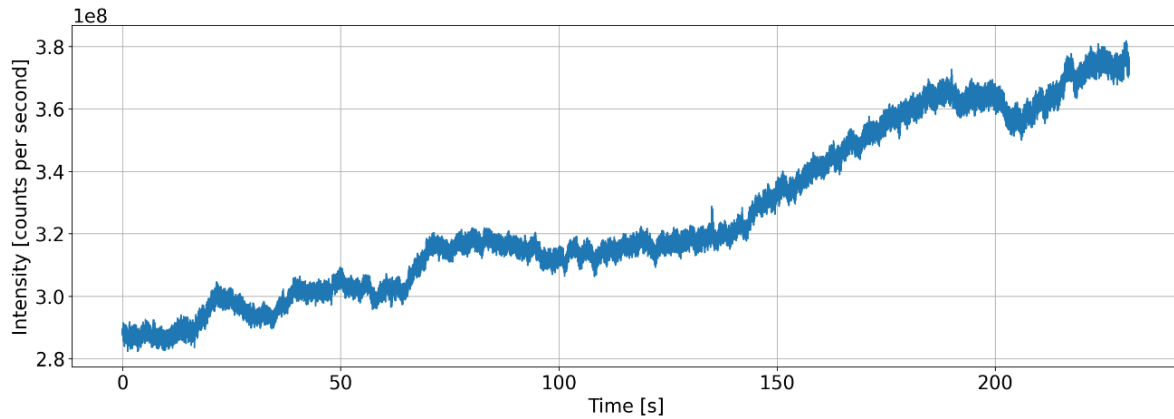
Figure 4.20: Inverted image taken with the dark-field microscope. The 1:100 diluted oil-in-water emulsion was imaged and two particles are visible, with the characteristic leaf shape, caused by the cross-polarization.

4.5.2 Emulsion actuation and analysis

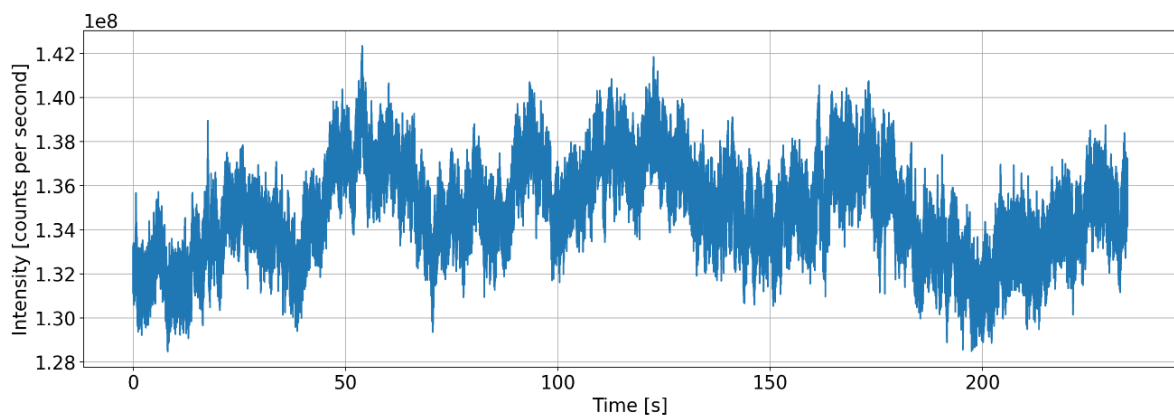
As mentioned in section 3.3, it is possible to apply a oscillating frequency and/or potential to a sample in the setup. After introducing the sample in the pipette, an immobilised single particle was searched in the FOV. Once a single particle has been located, an input (modulation) frequency and amplitude had to be selected. During the measurement, in which the frequency and amplitude are applied, the optical response in the form of a signal is recorded and stored. At the same time, the electronic signal is inspected with the oscilloscope, to ensure proper contact between the electrodes forming the circuit. Since the direction of the electric field is coming from top, the particle is actuated in the vertical direction.

First, a measurement is performed to test the stability and sensitivity of the optical setup, using an oil-in-water emulsion. The secondary laser, which is used to create a so-called drift-

lock/automatic feedback loop keeping the particle in the focus plane, is turned off. The resulting optical signal is shown in Figure 4.21a. After this, another emulsion particle was selected and the drift-lock was turned on. The result could be seen in Figure 4.21b. All intensities obtained in the dark-field setup have been divided by the camera exposure time (1 ms).



(a)



(b)

Figure 4.21: (a) No drift-lock, causing a large difference of the optical response of an oil-in-water emulsion droplet, actuated using a frequency of 163 Hz and an amplitude of 1 V. (b) The (smaller) intensity drift of an oil-in-water emulsion droplet, when kept in focus during the measurement. The particle is actuated using a frequency of 82 Hz and an amplitude of 15 V.

Now that we have established the need for a drift-lock, we apply different frequencies to a single emulsion droplet, while keeping the amplitude the same in between runs. Instead of comparing the different optical responses, we convert the signal into the frequency domain using again Fourier transformation. In this way, the modulation (input) frequency could be recovered, as well as any other frequency response obtained from the actuated particle.

For an oil-in-water emulsion, the resulting Fourier transformation is displayed in Figure 4.22. The powerspectrum (y-values) denotes how the intensity of a time-varying signal is distributed among the frequency domain.

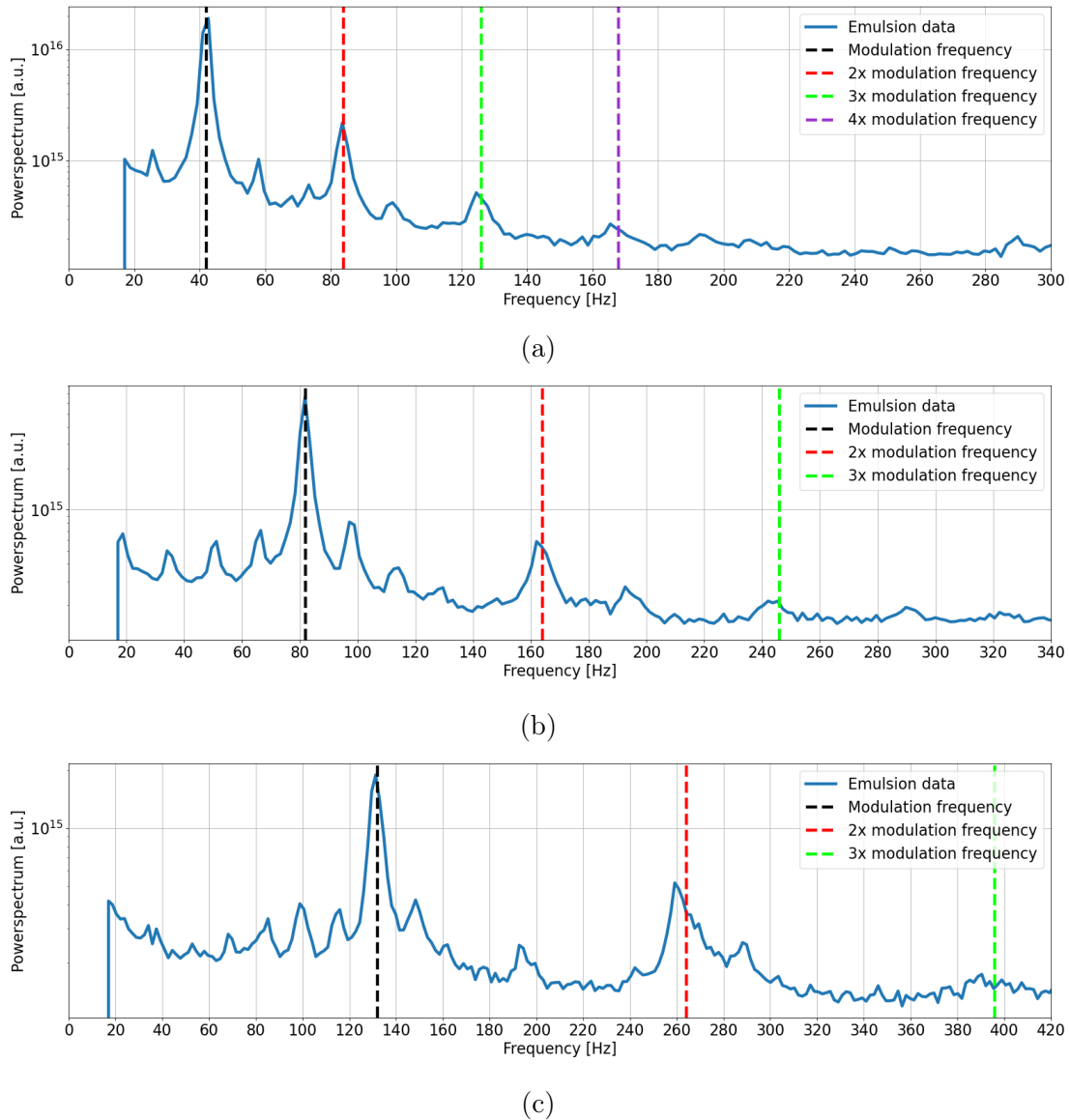
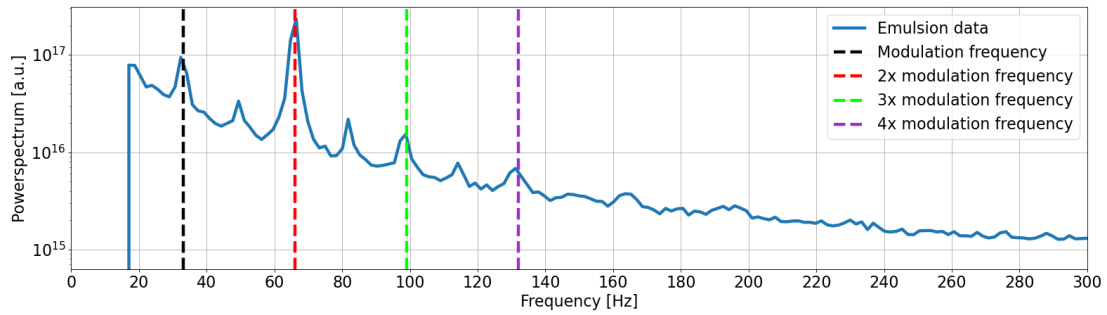


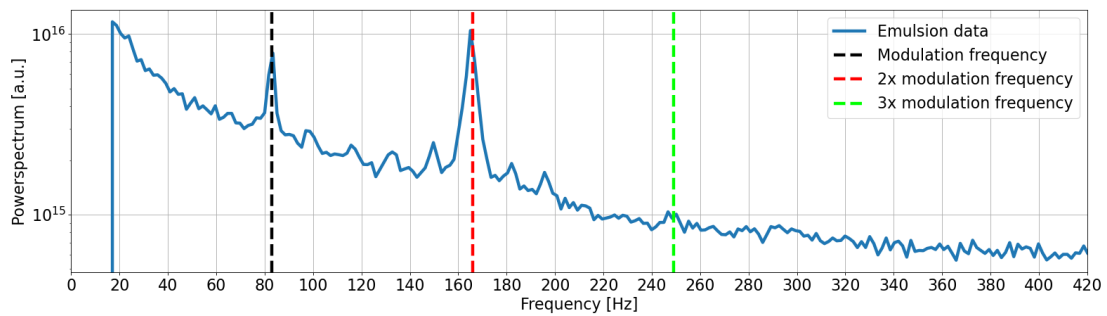
Figure 4.22: Fourier transformation of the optical signal of an oil-in-water emulsion droplet, during a measurement run in which a modulation frequency of (a) 42 Hz, (b) 82 Hz and (c) 132 Hz. An amplitude of 15 V is applied. Note that multiples of the modulation frequencies could be observed, as shown with the red, green and purple vertical lines.

The results shown in Figure 4.22 might serve as a starting point for further investigation, since not only the modulation frequency is observed, but also higher-order harmonics. This could be due to non-linear behaviour of the particle's motion under the influence of the applied electric field. At this point, both for the oil-in-water and water-in-oil (see next page), no hard conclusions about the particle response could be drawn, as there is no full understanding of why certain peaks arise, and for what frequency and amplitude.

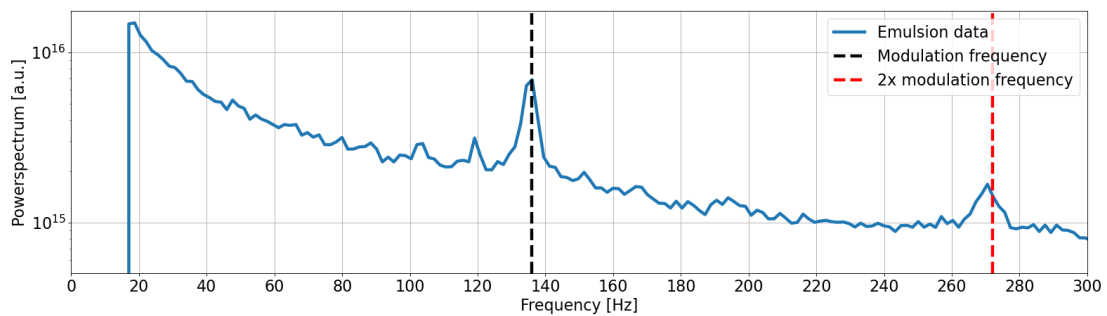
In addition to the actuation of an oil-in-water emulsion, the reverse composition, namely a water-in-oil emulsion droplet has been actuated in the dark-field microscope. Because oil is now the external phase, a higher amplitude could be used, compared to the 15 V used previously. The results of the Fourier transformation are shown in Figure 4.23.



(a)



(b)



(c)

Figure 4.23: Fourier transformation of the optical signal of a water-in-oil emulsion droplet, during a measurement run in which a modulation frequency of (a) 33 Hz, (b) 83 Hz and (c) 136 Hz. An amplitude of 200 V is applied. Note that multiples of the modulation frequencies could be observed, as shown with the red, green and purple vertical lines.

The water-in-oil results show a decreasing trend when looking at the powerspectrum values, which are yet to be explained. Repeated measurements with less/absent external disturbance might make this trend decrease. For both samples (oil-in-water and water-in-oil), the result after Fourier transformation shows a frequency cut-off around 18 Hz; since no frequencies are expected to occur below the modulation frequency, this is to filter out noise and other artifacts that might disturb the signal.

Chapter 5

Conclusion and outlook

In this work, first steps have been made to characterise nanoscopic particles using microscopy and computational analysis techniques. First of all, using bright-field microscopy, pre-defined polystyrene spheres and a self-made nanoemulsion have been studied. With a flow channel to create a thin-layer system in which the particle can diffuse, information about the studied particles could be obtained, such as their intensity. Using the intensity of known-sized spherical particles, an estimate was made of the particle size distribution of an oil-in-water emulsion, which turned out to be 128 ± 10 nm. In addition of using the intensity of particles in focus, out-of-focus fringe patterns might contain just as much relevance. Since the particle position and scattering profile are related, experimental fringes and simulated intensity fields have been compared using radial averaging and Fourier transformation. Although no direct comparisons are yet to be drawn, this might help in assigning the particle position in a layer system, potentially leading particle shape and concentration calculations.

Besides illumination in bright-field mode and tracking the particle intensity in 'regular' dispersed state, we also looked at a single emulsion droplet using dark-field microscopy. Single particles were actuated using an oscillating electric field and cross-polarization was used to obtain only light that has interacted with the particle, reducing the effect of (background) noise as much as possible. After testing the accuracy and stability of the setup, a single oil-in-water and water-in-oil emulsion droplet was actuated using various modulation frequencies, with a constant amplitude. The optical response was recorded and transformed using Fourier transformation. Besides the input frequency, higher-order harmonics were observed, potentially due to non-linear particle behaviour.

Follow-up

At the end of any research project, it is inevitable to think of next steps that could be taken with the knowledge obtained throughout this process. Some potentially interesting ideas are presented below:

1. Changing the composition of the prepared emulsion, for example more oil w.r.t the water, and keeping the preparation route the same, might give different sizes. It could be useful to find out how to create even smaller droplets, while avoiding an increase in instability (e.g., due to agglomeration).
2. Other properties besides the size, such as shape and displacement (e.g., diffusion constant) would assist in characterization of unknown particles. Here, the framework of analysing dispersed particles with trackpy might be of usage.
3. Lastly, the vast field of non-linear response could be unleashed on the first results obtained by actuating a single emulsion droplet. As the non-linear response gives a great fingerprint of the particle of study, it could be a powerful tool to study and resolve the structure of unknown, self-created particles.

Bibliography

- [1] G. Gaglia, S. Kabraji, D. Rammos, Y. Dai, A. Verma, S. Wang, C. Mills, M. Chung, J. Bergholz, S. Coy, J.-R. Lin, R. Jeselsohn, O. Metzger, E. Winer, D. Dillon, J. Zhao, P. Sorger, and S. Santagata, “Temporal and spatial topography of cell proliferation in cancer”, *Nature Cell Biology* **24**, 316–326 (2022).
- [2] C. Borrebaeck, “Precision diagnostics: moving towards protein biomarker signatures of clinical utility in cancer”, *Nature Reviews Cancer* **17**, 199–204 (2017).
- [3] G. Ma, Z. Wan, Y. Yang, P. Zhang, S. Wang, and N. Tao, “Optical imaging of single-protein size, charge, mobility, and binding”, *Nature communications* **11**, 4768 (2020).
- [4] V. Bayle, J.-B. Fiche, C. Burny, M. Platre, M. Nollmann, A. Martinière, and Y. Jaillais, “Single-particle tracking photoactivated localization microscopy of membrane proteins in living plant tissues”, *Nature Protocols* **16**, 1–32 (2021).
- [5] H. Xin, E. Dijk, S. Hall, J. Götte, N. Van Hulst, and H. Gersen, “Background-free detection of single 5 nm nanoparticles through interferometric cross-polarization microscopy”, *Nano Letters* **11**, 541–547 (2011).
- [6] D. Cole, G. Young, A. Weigel, and P. Kukura, “Label-free single-molecule imaging with numerical-aperture-shaped interferometric scattering microscopy”, *ACS Photonics* **4**, 211–216 (2016).
- [7] H. Shen, L. Tauzin, R. Baiyasi, W. Wang, N. Moringo, B. Shuang, and C. Landes, “Single particle tracking: from theory to biophysical applications”, *Chemical reviews* **117**, 7331–7376 (2017).
- [8] B. Brenner, K.-H. Song, C. Sun, and H. F. Zhang, “Improving spatial precision and field-of-view in wavelength-tagged single-particle tracking using spectroscopic single-molecule localization microscopy”, *Appl. Opt.* **60**, 3647–3658 (2021).
- [9] M. Imanbekova, S. Suarasan, Y. Lu, S. Jurchuk, and S. Wachsmann-Hogiu, “Recent advances in optical label-free characterization of extracellular vesicles”, *Nanophotonics* **11**, 2827–2863 (2022).
- [10] D. T. Kovari, D. Dunlap, E. R. Weeks, and L. Finzi, “Model-free 3d localization with precision estimates for brightfield-imaged particles”, *Opt. Express* **27**, 29875–29895 (2019).
- [11] S. L. Liu, J. Li, Z. L. Zhang, Z. G. Wang, Z. Q. Tian, G. P. Wang, and D. W. Pang, “Fast and high-accuracy localization for three-dimensional single-particle tracking”, *Scientific Reports* **3**, 2462 (2013).
- [12] Z. Ye, X. Wang, and L. Xiao, “Single-particle tracking with scattering-based optical microscopy”, *Analytical Chemistry* **91**, 15327–15334 (2019).
- [13] K.-H. Song, Y. Zhang, B. Brenner, C. Sun, and H. Zhang, “Symmetrically dispersed spectroscopic single-molecule localization microscopy”, *Light: Science & Applications* **9**, 92 (2020).
- [14] A. Malcolm, A. Dexter, and A. Middelberg, “Foaming properties of a peptide designed to form stimuli-responsive interfacial films”, *Soft Matter* **2**, 1057–1066 (2006).
- [15] M. Jaiswal, R. Dudhe, and P. Sharma, “Nanoemulsion: an advanced mode of drug delivery system”, *3 Biotech* **5**, 123–127 (2014).

-
- [16] A. D. Gadhave, “Nanoemulsions: formation, stability and application”, *Int. Journal for Research in Science & Advanced Technologies* **02**, 038–043 (2014), <https://tinyurl.com/3x6bk2fn>.
- [17] J. B. Aswathanarayan and R. R. Vittal, “Nanoemulsions and their potential applications in food industry”, *Frontiers in Sustainable Food Systems* **3**, 1–21 (2019).
- [18] W. H. Hoffmann, “Development of nanoparticle tracking analysis for advanced nanoparticle characterisation in dispersions”, PhD thesis (The University of Bristol, 2022), <https://hdl.handle.net/1983/fede89a0-9c6e-4303-8183-c0514c696ad1>.
- [19] D. Clements, “Characterization of emulsion properties”, in *Food emulsions: principles, practices and techniques*, Vol. 2 (CRC Press, 2005).
- [20] T. J. Ashaolu, “Nanoemulsions for health, food, and cosmetics: a review”, *Environmental Chemistry Letters* **19**, 3381–3395 (2021).
- [21] K. Yao and J. Shen, “Measurement of particle size and refractive index based on interferometric particle imaging”, *Optics & Laser Technology* **141**, 107110 (2021).
- [22] L. Qieni, H. Kan, G. Baozhen, and W. Xiang, “High-accuracy simultaneous measurement of particle size and location using interferometric out-of-focus imaging”, *Opt. Express* **24**, 16530–16543 (2016).
- [23] C. Shen, Z. Jiang, L. Li, J. F. Gilchrist, and H. D. Ou-Yang, “Frequency response of induced-charge electrophoretic metallic janus particles”, *Micromachines* **11**, 1–14 (2020).
- [24] F. Lickert, H. Bruus, and M. Rossi, “Constant-power versus constant-voltage actuation in frequency sweeps for acoustofluidic applications”, *Micromachines* **13**, 1–16 (2022).
- [25] D. Serantes, R. Chantrell, H. Gavilán, M. d. P. Morales, O. Chubykalo-Fesenko, D. Baldomir, and A. Satoh, “Anisotropic magnetic nanoparticles for biomedicine: bridging frequency separated ac-field controlled domains of actuation”, *Phys. Chem. Chem. Phys.* **20**, 30445–30454 (2018).
- [26] P. Von Olshausen and A. Rohrbach, “Coherent total internal reflection dark-field microscopy: label-free imaging beyond the diffraction limit”, *Opt. Lett.* **38**, 4066–4069 (2013).
- [27] J. Bailleul, B. Simon, M. Debailleul, and O. Haeberlé, “An introduction to tomographic diffractive microscopy: toward high-speed quantitative imaging beyond the abbe limit”, in *Micro- and nanophotonic technologies* (Wiley-VCH Verlag GmbH, 2017).
- [28] B. T. Miles, E. C. Robinson, E. M. H. P. van Dijk, I. D. Lindsay, N. F. van Hulst, and H. Gersen, “Sensitivity of interferometric cross-polarization microscopy for nanoparticle detection in the near-infrared”, *ACS Photonics* **2**, 1705–1711 (2015).
- [29] D. Langevin, “Light scattering by liquid surfaces, new developments”, *Advances in Colloid and Interface Science* **289**, 102368 (2021).
- [30] D. Williams and C. Carter, “Lenses, apertures, and resolution”, in *Transmission electron microscopy*, Vol. 3 (Springer New York, NY, 2009).
- [31] A. Gupta, B. Eral, T. Hatton, and P. Doyle, “Nanoemulsions: formation, properties and applications”, *Soft Matter* **12**, 2826–2841 (2016).
- [32] A. Horalchuk, O. Grinchenko, O. Riabets, and O. Kotlyar, “Food dispersion systems process stabilization. a review”, *Ukrainian Food Journal* **8**, 699–732 (2019).
-

-
- [33] J. Callejas-Fernández, J. Ramos, O. Sanz, J. Forcada, J. L. Ortega-Vinuesa, A. Martín-Molina, M. A. Rodríguez-Valverde, M. Tirado-Miranda, A. Schmitt, B. Sierra-Martin, A. Maldonado-Valdivia, A. Fernández-Barbero, R. Pons, L. F. Capitán-Vallvey, A. Salinas-Castillo, A. Lapresta-Fernández, B. Vázquez, M. R. Aguilar, and J. San Román, “Experimental techniques used for the characterization of soft nanoparticles”, in *Soft nanoparticles for biomedical applications* (The Royal Society of Chemistry, 2014).
- [34] J. M. Oh, S. H. Ko, and K. H. Kang, “Shape oscillation of a drop in ac electrowetting”, *Langmuir* **24**, 8379–8386 (2008).
- [35] R. Wilson, Y. Li, G. Yang, and C.-X. Zhao, “Nanoemulsions for drug delivery”, *Partic-uology* **64**, 85–97 (2022).
- [36] M. Belhaq, in *Recent trends in applied nonlinear mechanics and physics: selected papers from csnndd 2016* (Springer, 2018).
- [37] H. Yong, D. Meng, W. Zuo, and L. Zhang, “Robust online matrix factorization for dynamic background subtraction”, *IEEE Transactions on Pattern Analysis and Machine Intelligence* **40**, 1726–1740 (2018).
- [38] J. C. Crocker and D. G. Grier, “Methods of digital video microscopy for colloidal studies”, *Journal of Colloid and Interface Science* **179**, 298–310 (1996).
- [39] A. Oppenheim and J. Lim, “The importance of phase in signals”, *Proceedings of the IEEE* **69**, 529–541 (1981).
- [40] A. Egel, K. Czajkowski, D. Theobald, K. Ladutenko, A. Kuznetsov, and L. Pattelli, “Smuthi: a python package for the simulation of light scattering by multiple particles near or between planar interfaces”, *Journal of Quantitative Spectroscopy and Radiative Transfer* **273**, 107846 (2021).
- [41] W. Wiscombe, “Mie scattering calculations: advances in technique and fast, vector-speed computer codes”, National center for atmospheric research, 1–98 (1979).
- [42] S. Faez, A. Carattino, and A. Mosk, “Pynta: an open source software application for live particle tracking”, *Preprints*, 10.20944/preprints201906.0251.v1 (2019).

Appendix A

Pixel size calibration

A.1 Bright-field microscope

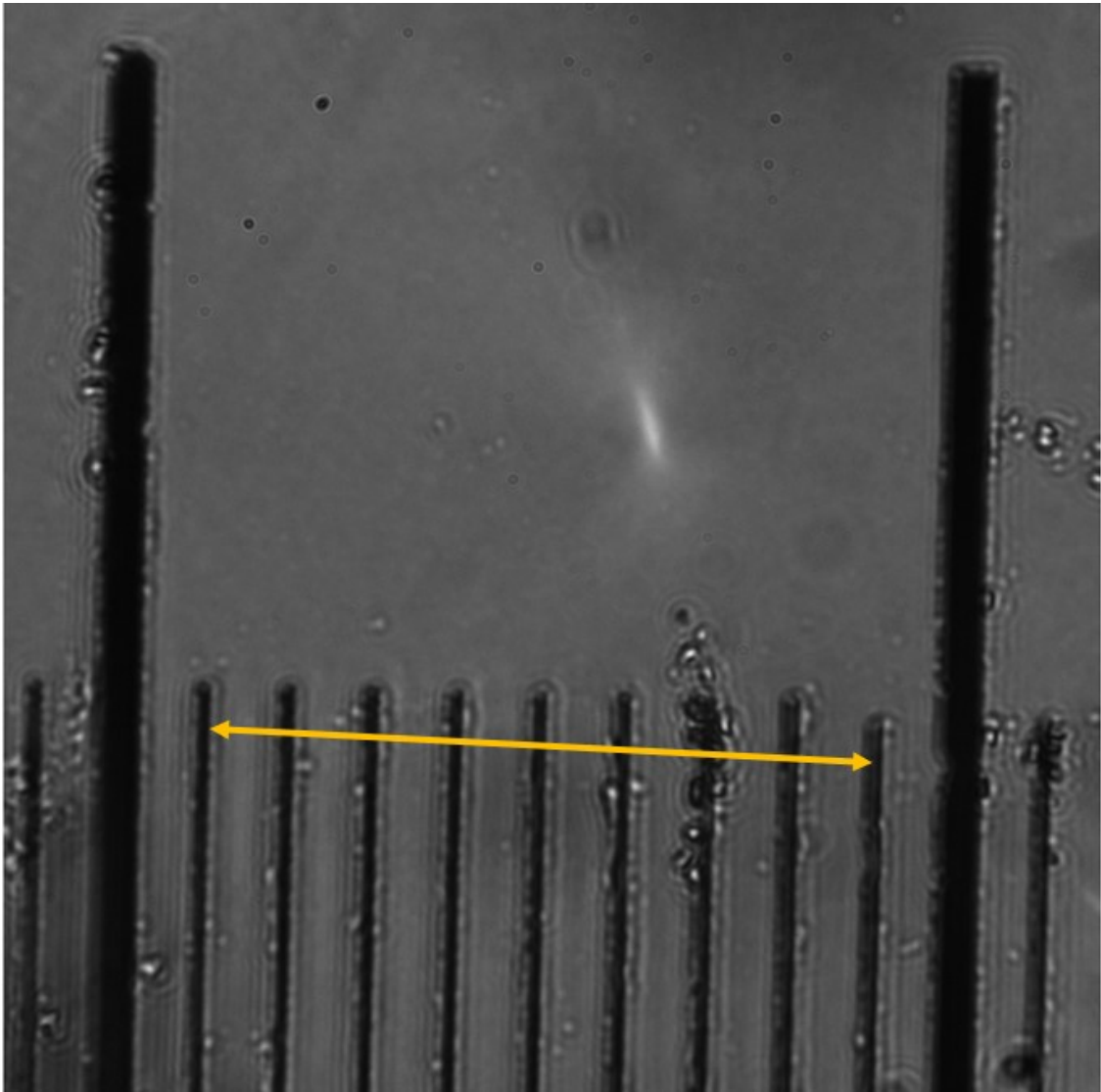


Figure A.1: Bright-field microscope calibration. A full-size image was taken with the set up, corresponding to 2048x2048 effective pixels. The ruler (Thorlabs R1L3S2P) has 100 μm divisions between the large black stripes and 10 μm separation between the thinner stripes. The yellow line covers 8 divisions, corresponding to 80 μm and has a pixel length of 1256. This results in a pixel size of 64 nm.

A.2 Dark-field microscope

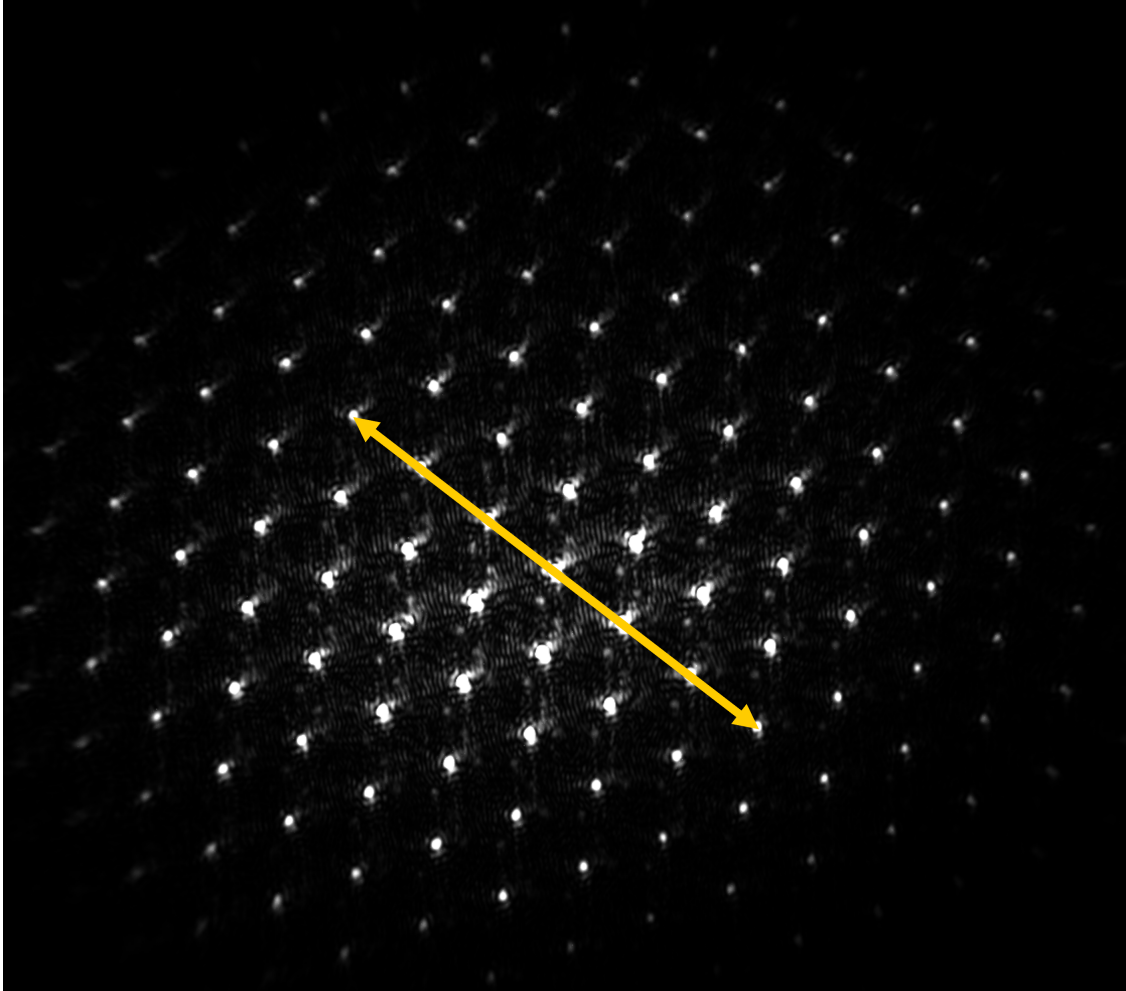


Figure A.2: Dark-field microscope calibration. Using evaporation, gold was deposited and a mask was created. The distance between bright spots corresponds to $4.5\ \mu\text{m}$. The yellow line covers 6 separations, corresponding to $27\ \mu\text{m}$. The pixel length of this line is 540, which makes the pixel size equal to 50 nm.

Appendix B

Data and code availability

All analysis scripts and simulation codes used in this work could be found on gitlab. The experimental data is available on request. Three of the used scripts are displayed in the following sections.

B.1 Comparison of extinction efficiency calculated with SMUTHI and Miepython

```
1 import numpy as np
2 import matplotlib.pyplot as plt
3 import smuthi.simulation
4 import smuthi.initial_field
5 import smuthi.layers
6 import smuthi.particles
7 import smuthi.postprocessing.far_field as ff
8 import miepython
9 from matplotlib.pyplot import figure
10
11 # In this file, all lengths are given in nanometers
12
13 def mie_reference(ni, no):
14
15     """
16     generate the Mie crosssection for a fix range
17
18     return:
19         x : sphere diameters
20         q : extinction efficiencys
21     """
22     x = np.linspace(40, 10000, 400)
23     qext, qsca, qback, gcos = miepython.ez_mie(ni, x, 550, n_env = no)
24     return x, qsca
25
26 # Initialize the layer system object
27
28 # Refractive indices: glass: 1.52, water: 1.333, PS:1.5916 , octane
29     =1.3989,
30 # Tween-20=1.468
31 three_layers = smuthi.layers.LayerSystem(thicknesses=[0, 20000, 0],
32     refractive_indices=[1.52, 1.333,
33     1])
34 sph_size = np.linspace(20, 10000, 400)
35
36
37 sc_sect = 0*sph_size
38 i = 0
```

```

39
40 for r in sph_size:
41 # Scattering particle
42     sphere = smuthi.particles.Sphere(position=[0, 0, 2000],
43                                     refractive_index=1.5916,
44                                     radius=r,
45                                     l_max=1)
46
47 # list of all scattering particles (only one in this case)
48     one_sphere = [sphere]
49
50 # Initial field
51     plane_wave = smuthi.initial_field.PlaneWave(vacuum_wavelength=550,
52                                                  polar_angle=0*np.pi, # from
53                                                  azimuthal_angle=0,
54                                                  polarization=0) # 0=TE
55
56     l=TM
57
58 # Initialize and run simulation
59     simulation = smuthi.simulation.Simulation(layer_system=three_layers,
60                                             particle_list=one_sphere,
61                                             initial_field=plane_wave)
62
63     simulation.run()
64
65 # evaluate the scattering cross section
66     scs = ff.total_scattering_cross_section(initial_field=plane_wave,
67                                           particle_list=one_sphere,
68                                           layer_system=three_layers)
69
70     sc_sect[i] = scs/(np.pi*r**2)
71     i = i+1
72     print(r, "nm sphere done!")
73
74 x, qsca = mie_reference(1, 1.333)
75
76 plt.rcParams['font.size'] = 16
77
78 figure(figsize=(10,10))
79 plt.loglog(x/2, qsca, '.-', label='Mie python package', linewidth=4)
80 plt.loglog(sph_size, sc_sect, '.-', label='SMUTHI package', linewidth=4)
81
82 plt.xlabel('Sphere radius [nm]')
83 plt.ylabel('Extinction efficiency coefficient')
84 plt.legend()
85 plt.grid()
86 plt.show()

```

B.2 Determining the accuracy of a SMUTHI extinction efficiency calculation

```

1 import numpy as np
2 import matplotlib.pyplot as plt
3 import smuthi.simulation
4 import smuthi.initial_field
5 import smuthi.layers
6 import smuthi.particles

```

```

7 import smuthi.postprocessing.far_field as ff
8 from matplotlib.pyplot import figure
9
10 # In this file, all lengths are given in nanometers
11
12 # Initialize the layer system object
13
14 # Refractive indices: glass: 1.52, water: 1.333, PS:1.5916 , octane
    =1.3989,
15 # Tween-20=1.468
16
17 three_layers = smuthi.layers.LayerSystem(thicknesses=[0, 20000, 0],
18                                           refractive_indices=[1.52, 1.333,
    1])
19 sph_size = np.linspace(20, 10000, 400)
20
21 sc_sect = 0*sph_size
22 i = 0
23
24 for r in sph_size:
25 # Scattering particle
26     sphere = smuthi.particles.Sphere(position=[0, 0, 2000],
27                                       refractive_index=1.5916,
28                                       radius=r,
29                                       l_max=12) # vary 1 or 6 or 12
30
31 # list of all scattering particles (only one in this case)
32     one_sphere = [sphere]
33
34 # Initial field
35     plane_wave = smuthi.initial_field.PlaneWave(vacuum_wavelength=550,
36                                                  polar_angle=1*np.pi, # vary 0
    or 1
37                                                  azimuthal_angle=0,
38                                                  polarization=0) # 0=TE
    wave
39
40 # Initialize and run simulation
41     simulation = smuthi.simulation.Simulation(layer_system=three_layers,
42                                             particle_list=one_sphere,
43                                             initial_field=plane_wave)
44     simulation.run()
45
46 # evaluate the scattering cross section
47     scs = ff.total_scattering_cross_section(initial_field=plane_wave,
48                                             particle_list=one_sphere,
49                                             layer_system=three_layers)
50     sc_sect[i] = scs/(np.pi*r**2)
51     i = i+1
52     print(r, "nm sphere done!")
53
54 plt.rcParams['font.size'] = 16
55
56 figure(figsize=(10,10))
57 plt.loglog(sph_size, sc_sect, '.-', color='orange', linewidth=4)
58 plt.xlabel('sphere radius [nm]')
59 plt.ylabel('Extinction efficiency coefficient')
60 plt.grid()

```

```
61 plt.show()
```

B.3 SMUTHI scattering profiles for varying particle positions in a layer system

```

1 import numpy as np
2 import smuthi.simulation
3 import smuthi.initial_field
4 import smuthi.layers
5 import smuthi.particles
6 import smuthi.postprocessing.graphical_output as go
7 import smuthi.utility.cuda
8
9 # In this file, all lengths are given in nanometers
10 three_layers = smuthi.layers.LayerSystem(thicknesses=[0, 15000, 0],
11                                           refractive_indices=[1.52, 1.333,
12                                           1])
13 # defining range of simulation parameters
14 sph_r = 200 #base sphere radius in nanometers
15
16 # Scattering particles, immersed in the water layer
17 sphere = smuthi.particles.Sphere(position=[0, 0, 11000], # vary z-position
18                                   refractive_index=1.5916,
19                                   radius=200,
20                                   l_max=6)
21
22 # Initial field
23 plane_waveTE = smuthi.initial_field.PlaneWave(vacuum_wavelength=550,
24                                                polar_angle=0.0*np.pi,
25                                                azimuthal_angle=0,
26                                                polarization=0) # 0=TE 1=TM
27
28 plane_waveTM = smuthi.initial_field.PlaneWave(vacuum_wavelength=550,
29                                                polar_angle=0.0*np.pi,
30                                                azimuthal_angle=0,
31                                                polarization=1) # 0=TE 1=TM
32
33 # list of all scattering particles (only one in this case)
34 one_particle = [sphere]
35
36 # Initialize and run simulation
37 simulationTE = smuthi.simulation.Simulation(layer_system=three_layers,
38                                             particle_list=one_particle,
39                                             initial_field=plane_waveTE,
40                                             length_unit='nm')
41 simulationTE.run()
42
43
44 simulationTM = smuthi.simulation.Simulation(layer_system=three_layers,
45                                             particle_list=one_particle,
46                                             initial_field=plane_waveTM,
47                                             length_unit='nm')
48 simulationTM.run()
49
50 # Create plots that visualize the electric near field.
```

```
51
52 go.show_near_field(quantities_to_plot=['E_x'],
53                    show_plots=True,
54                    show_opts=[{'label': 'raw_data'}],
55                    save_opts=[{'format': 'png'}],
56                    save_data=True,
57                    save_plots=True,
58                    outputdir='./testIngmar/D_data/thickness15um/r200nm/E_x
    /',
59
60                    xmin=-5500,
61                    xmax=5500,
62                    ymin=-5500,
63                    ymax=5500,
64                    zmin=-100,
65                    zmax=-100,
66                    resolution_step=75,
67                    simulation=simulationTM,
68                    show_internal_field=True)
69
70 go.show_near_field(quantities_to_plot=['E_y'],
71                    show_plots=True,
72                    show_opts=[{'label': 'raw_data'}],
73                    save_opts=[{'format': 'png'}],
74                    save_data=True,
75                    save_plots=True,
76                    outputdir='./testIngmar/D_data/thickness15um/r200nm/E_y
    /',
77
78                    xmin=-5500,
79                    xmax=5500,
80                    ymin=-5500,
81                    ymax=5500,
82                    zmin=-100,
83                    zmax=-100,
84                    resolution_step=75,
85                    simulation=simulationTE,
86                    show_internal_field=True)
```